

Design and Development of Linac-MR Hybrids

*B. Gino Fallone, Ph.D., Brad Murray, MSc, Ben Burke, Ph.D., Amir Keyvanloo, Ph.D.,
Satyapal Rathee, Ph.D., Joel St. Aubin, Ph.D., Stephen Steciw, Ph.D.,
Keith Wachowicz, Ph.D., Brad Warkentin, Ph.D., and Jihyun Yun, Ph.D.*

*Cross Cancer Institute
University of Alberta
Edmonton, Alberta, Canada*

6.1	Introduction	114
6.2	The Linac and MRI Hybrid Hardware.....	116
6.2.1	Need for Linac-MR Hybrids	116
6.2.2	Simulating the Linac and Electron Gun	116
6.2.3	Commissioning the Integrated Linac Model.....	117
6.2.4	Effect of the Magnetic Field on Linac Operation.....	118
6.2.5	Magnetic Decoupling of the Linac from the MRI.....	119
6.2.6	Short 10 MV Linac Development.....	120
6.2.7	Linear Accelerator Effects on MRI RF Coils	122
6.3	Radiation Dosimetry in Magnetic Fields	124
6.3.1	In-patient Dosimetry	125
6.3.2	Surface Dose.....	128
6.3.3	Deterministic Dose Calculations in Magnetic Fields.....	129
6.3.4	Response of Radiation Detectors in Magnetic Fields	131
6.4	Intra-Fractional Tumor-Tracked Irradiation	133
6.4.1	Overview of Intra-fractional Tumor Tracking	133
6.4.2	Proof of Concept: Linac-MR Tumor-tracked Irradiation	134
6.5	MR Imaging for Radiotherapy	136
6.5.1	Geometric Image Distortion: Overview	136
6.5.2	General Correction Methodology	137
6.6	Conclusions.....	140
6.7	References.....	140

6.1 Introduction to MRI-to-linac Hybrid Integration

Directly or indirectly, cancer will affect everyone's life. Radiotherapy (RT) is integral to the management and treatment of many cancers, and while it has evolved dramatically, current delivery continues to be limited by inherent soft tissue motion. Respiration, cardiac pulsations, peristalsis, and filling of the stomach, bladder, and rectum can significantly affect the shape and motion of the tumor and nearby structures. To account for motion both during the treatment delivery and between subsequent treatment fractions, radiation is delivered to a much larger volume, within which the tumor is expected to move. As a result of this target expansion, the irradiated volume necessarily includes normal tissues, leading to undesirable side effects. Short-term effects may resolve with time, while long-term side effects can take years to present, but they are usually permanent and may involve significant morbidity.

The implication of motion on RT outcomes has been recognized for decades, and considerable efforts have been focused on image-guided radiation therapy (IGRT) and image-guided adaptive radiotherapy (IGAR) to reduce the uncertainty in tumor position and decrease the volume of normal tissue irradiated. Daily images are acquired immediately preceding treatment to adjust patient setup and reduce uncertainty in the tumor location. If sufficient changes in tumor shape or location are observed, the treatment can be suspended and a new plan developed. Current state-of-the-art IGRT and IGAR systems primarily rely on x-ray-based technology—flat panel imagers, megavoltage computed tomography (MVCT), and cone-beam computed tomography (CBCT). These techniques increase the patient dose outside the treatment volume and cannot provide 3D real-time imaging during treatment. Although alignment to

soft tissue visualized in MVCT or in CBCT can be performed, this process is difficult due to poor soft tissue contrast provided by x-ray-based systems. Alternatively, patient setup can be adjusted based on the location of bony landmarks or implanted fiducial markers. Except for bone, all solid tumors occur within soft tissue and may deform or move with respect to the skeleton (Case et al. 2009). Surrogates must be surgically implanted, but they cannot provide volumetric information and may not accurately represent tumor position. The IMRIS (Chanhassen, MN) technology is an attempt to overcome the limitations of x-ray-based imaging with an MRI that moves in and out of an RT vault prior to treatment to visualize patient setup. Although distinct from IMRIS, our IGAR program (circa 2002) at the Cross Cancer Institute (CCI) performed a similar function by moving the patient on a couch between a 3 T MR imaging suite and the nearby TomoTherapy (Sunnyvale, CA) unit for treatment (Fallone 2003; Sinha et al. 2005).

Despite improvements in IGRT and IGAR, all current technology prohibits the intra-fraction real-time 3D volumetric imaging that is required to track tumor and organ motion, decrease treatment margins, and improve patient outcomes. The ideal image guidance system would provide (1) soft tissue contrast and spatial resolution sufficient to differentiate tumor tissue from surrounding normal tissues, (2) real-time image acquisition, and (3) adaptation of radiation delivery to real-time tumor motion and deformation. A natural resolution to this problem would be to integrate a radiation therapy delivery device, such as a linear accelerator (linac), with a magnetic resonance imaging (MR) system and thus overcome the complex issue of motion management by offering the three key features mentioned above. The integrated hybrid (linac-MR) would accurately track the tumor position at all times before and during the

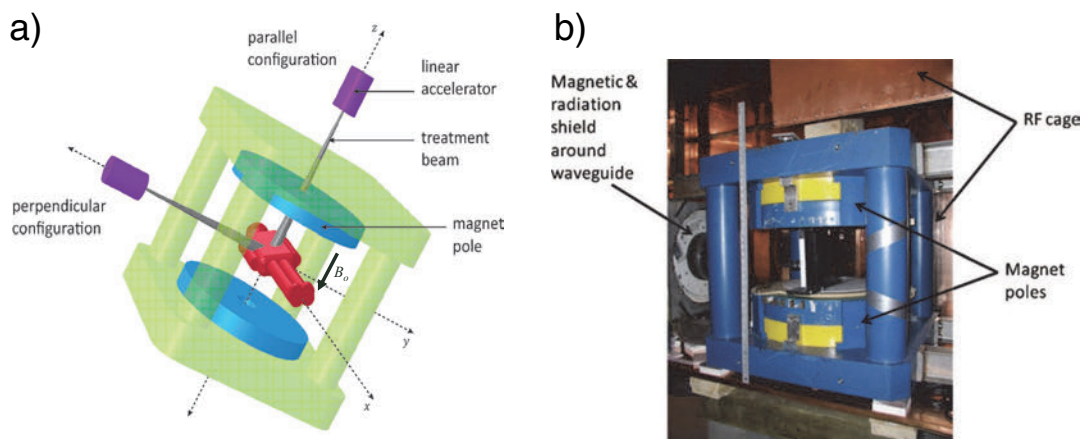


Figure 6–1. a) Schematic of rotating bi-planar MR combined with a linac. The B_0 magnetic field runs between the poles as shown. The central axis of the linac can be positioned/configured either perpendicular or parallel to B_0 . b) Taken during the construction of Phase I system: bi-planar magnet in blue with flat gradients in perpendicular configuration. The 0.25 T magnet is physically connected to a cylindrical magnetic shield assembly surrounding a 6 MV Varian 600C waveguide. The dark instrument inside the magnet is a “jig” to measure the magnetic field distributions inside the MR magnet used in the shimming process of the magnet. From (Fallone et al. 2009) and www.linac-MR.ca.

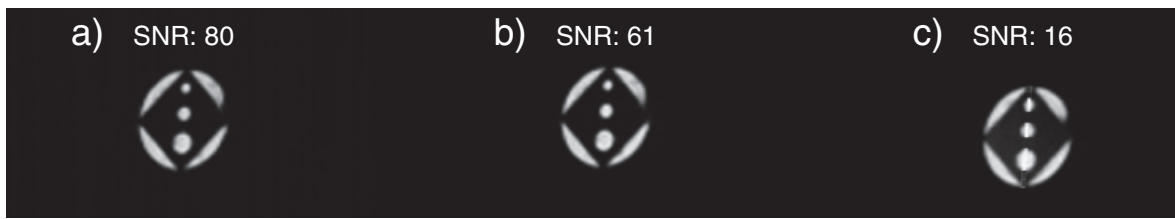


Figure 6–2. Images from the setup shown in Figure 6–1 are obtained with a gradient echo sequence, flip angle = 90.0° , TE = 14 ms, TR = 300 ms, bandwidth = 10 kHz, slice thickness = 7 mm, matrix size = 128×128 , FOV = $100 \times 100 \text{ mm}^2$, and number of averages = 1. Each image was obtained in 38 s. Image a) is obtained with linac powered up without beam on, b) with radiation pulse outside the acquisition window, and c) with radiation pulse inside the acquisition window. Note that the effective RF shielding design had not been implemented at the time of this experiment in 2008, and thus explains the reduction in SNR. This is the first worldwide set of MR images of a phantom while being irradiated by a linac. From (Fallone et al. 2009.)

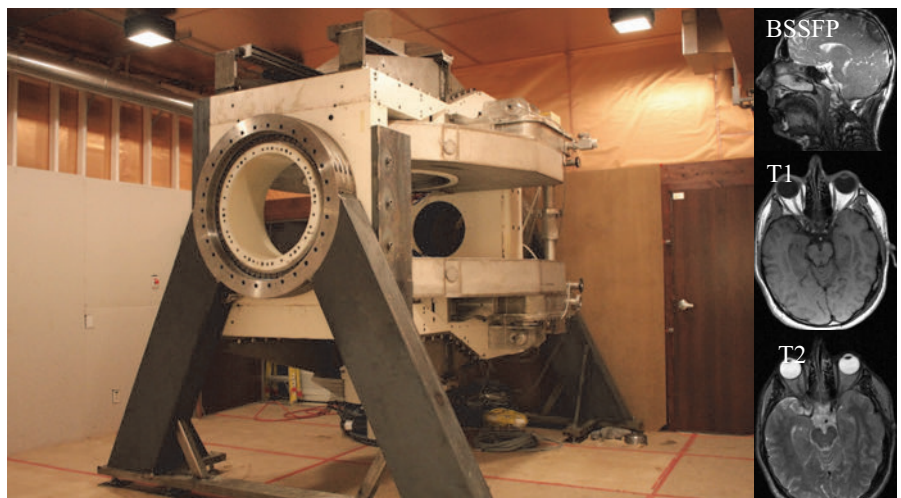
treatment, conform the radiation beam to the moving tumor, and maximize normal tissue avoidance. In doing so, it would increase loco-regional tumor control and reduce side effects, thereby improving the survival and long-term health of cancer patients.

Development of a combined MR/radiation delivery system represents a significant technical challenge. Concurrent research is being undertaken by several international groups. Dempsey et al. (2005) have combined a stationary 0.35 T split coil MRI system with three Cobalt-60 (^{60}Co) sources. The use of ^{60}Co results in larger penumbra, higher surface dose, reduced radiation penetration, and lower dose rates than a typical modern radiotherapy linear accelerator (Khan 2003). Lagendijk et al. (2008) have combined a 6 MV linac with a 1.5 T MRI, irradiating through the magnet structure. Although they have demonstrated proof of concept with this design, the alteration of in-patient dose at such high field strengths is significant in lung and in skin (Kirkby et al. 2010; 2008).

The Cross Cancer Institute in Edmonton has developed a rotating bi-planar linac-MR device which resolves some of these issues (Fallone 2007). The MR is an open bi-planar magnet

where the main magnetic field runs from one plane to the other (Figure 6–1a). The linac is placed such that the therapeutic radiation beam traverses between the two planes (perpendicular configuration) or through the central opening of one of the two plane coils (parallel configuration). The linac waveguide and the MR rotate in unison to the angle of treatment (Fallone et al. 2009; St. Aubin et al. 2010). The development followed a three-phased research approach (peer-reviewed articles available from linacMR.ca/publications.html). The first phase involved the proof-of-concept prototype shown in figures 6–1b and 6–2, which combined a 6 MV linac with a head-sized (30 cm patient gap) permanent 0.25 T magnet to be first in delivering linac radiation during MRI acquisition (Fallone et al. 2009). The second phase, shown in Figure 6–3, is our V.1, which interfaced a 6 MV linac with a superconducting whole-body 0.5T MR system (60 cm patient gap) to demonstrate the structural and mechanical integrity of the system on a scaled-up rotating gantry (Fallone 2014; Santos et al. 2012). The third phase, shown in Figure 6–4, is our V.2 (Aurora-RTTM, MagnetTx Oncology Solutions, Edmonton, Canada; www.magnetTx.com) which involves a 6 MV linac integrated with a highly compact whole-body

Figure 6–3. The second phase involves V.1 shown in the figure, of the whole-body rotating linac-MR installed through the maze of an existing vault (depth: 19.4 ft, width: 19.8 ft, height: 12 ft.) at the Cross Cancer Institute, Edmonton, Alberta, Canada in 2013. The MRI includes a 0.5 Tesla high-temperature superconducting magnet with a 60 cm diameter bore that does not require any cryogenics or exhaust vent. The linac is a 6 MV Varian 600C. The gantry rotates at 1 revolution/minute. Right: typical MR images on a volunteer (July 2014). From www.linacMR.ca.



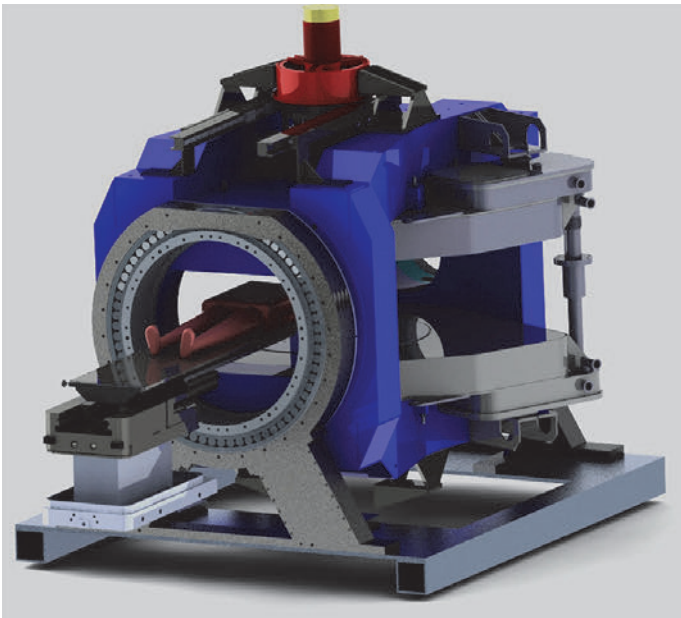


Figure 6-4. The third phase involves V.2 shown in the figure of the whole-body rotating linac-MR with a 110 cm by 60 cm patient-bore gap. From www.linacMR.ca.

superconducting 0.5 T MRI with optimal homogeneity, structural rigidity, a user-friendly integrated console, and a 110 cm × 60 cm patient opening that allows for significant lateral motion of the couch within the “open” section of the MRI. The last feature allows for accurate treatment of peripheral tumors by moving the planned treatment volume to the isocenter for optimum MR imaging and treatment for each treatment angle. To avoid collisions between the couch and the system during rotation, the center of the patient is re-placed at the system’s isocenter during rotation.

The following pages described the physics and engineering aspects of hybrid linac-MR designs, in particular, those associated with the rotating bi-planar linac-MR system.

6.2 The Linac and MRI Hybrid Hardware

6.2.1 Challenges Merging a Linac to an MRI

Integrating a magnetic resonance imaging (MRI) scanner and medical linear accelerator (linac) poses unique challenges for electron acceleration within the linac accelerating waveguide. Due to its close proximity to the MRI scanner, the linac is immersed in the fringe magnetic field of the MRI, causing a Lorentz force to act on the electrons accelerating within the waveguide. Standard linac operation accelerates low-energy electrons to very high energies in a straight line. Therapeutic x-rays are generated as the high-energy electrons interact with a metal target placed at the end of their accelerating path through Bremsstrahlung interactions, a process in which the electrons convert some of their kinetic energy to x-rays through radiative

losses. Without appropriate magnetic shielding, the electrons will be deflected from their straight path to the target, causing a reduction in x-ray output and changes to important dosimetric parameters, such as radiation beam symmetry. Depending on the fringe field orientation with respect to the accelerating electrons, all useful radiation output can be completely lost, even with quite low magnetic field magnitudes. By understanding the effect of magnetic fields on linac operation, optimized magnetic shielding can be designed that guarantees proper operation of the linac, while also ensuring minimal perturbations in the homogeneity of the MRI needed for undistorted imaging.

6.2.2 Simulating the Linac and Electron Gun

Investigations into the effect of the magnetic fields on the linac began with the creation of a simulated linac. The dimensions of a published accelerating cavity (Roy and Shanker 1993) were redesigned using the widely benchmarked two-dimensional (2D) conformal finite difference program SUPERFISH (Los Alamos National Laboratory, NM) (Halbach and Holsinger 1976) in order to emulate the Varian™ 600C waveguide, the accelerator used in the first linac-MR systems at the Cross Cancer Institute in Edmonton, AB, Canada. COMSOL (Multiphysics, Burlington, MA) was then used to generate the three-dimensional (3D) linac accelerator model, whose schematic is shown in Figure 6-5, using the Finite Element Method (FEM) (Jin 2002). The 3D COMSOL linac model was validated against SUPERFISH in order to ensure accuracy in the 3D simulations (St. Aubin et al. 2010a). The electron acceleration and resultant trajectories were calculated based on the 3D electromagnetic fields of COMSOL using the 3D particle-in-cell calculations of the PARMELA software (Los Alamos National Laboratories, NM).

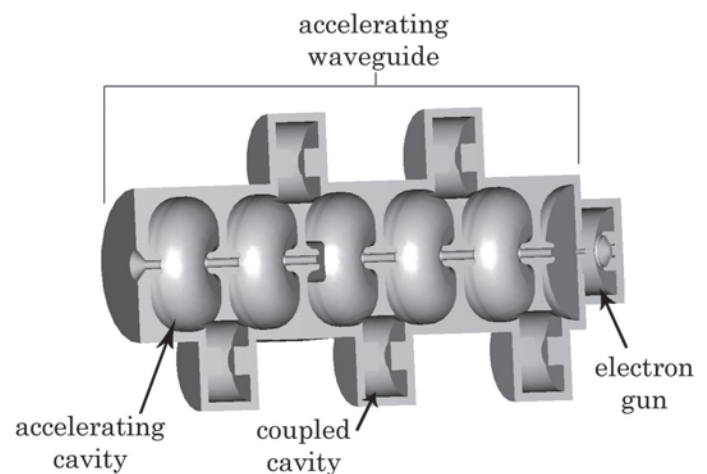


Figure 6-5. Schematic cutaway section of the simulated linear accelerator waveguide and electron gun. From (St. Aubin et al. 2010a).

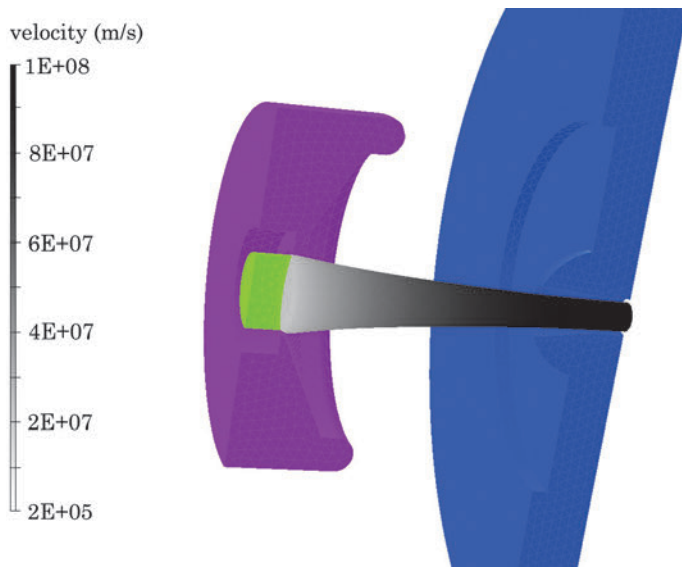


Figure 6–6. The geometry of the 3D SCALA electron gun with the relativistic electron velocities. Only half of the geometry is shown with the anode on the right, the focusing electrode on the left, and the cathode defined by the location of electron emission. From (St. Aubin et al. 2010c).

A significant result of this work showed that the electric field magnitude could be adjusted by adjusting the coupling port size of the first accelerating half-cavity into which the electrons are injected. The magnitude of the electric field in the first cavity was found to play a major role in the capture efficiency of the electrons injected from the electron gun and in the final focal spot size at the target.

A novel electron gun—which injects electrons into the accelerating waveguide via thermionic emission and strong

electrostatic fields—was also developed based on measurements taken from the electron gun on a Varian™ 600C waveguide (St. Aubin et al. 2010d). The electron gun was initially modeled in 2D (St. Aubin et al. 2010d) using the EGN2w software (Stanford Linear Accelerator Center, CA), and ultimately in 3D (St. Aubin et al. 2010c) using OPERA-3D/SCALA software (Figure 6–6). With the electron gun designed according to measurements, the full 3D linac simulation could be commissioned. The final 3D electron gun that was designed according to Varian™ 600C specifications had a current output that was calculated to be 0.361 ± 0.002 A.

6.2.3 Commissioning the Integrated Linac Model

Commissioning was performed by running various linac simulations that provided a six-dimensional (6D) phase space at the location of the target. The EGSnrc (Kawrakow et al. 2009; Rogers et al. 1995) radiation transport codes were used for the Monte Carlo calculations using the 6D phase space as an input. An iterative approach was taken to commission the final simulated linac design by changing certain parameters in the simulated linac design until the calculated dosimetric profiles and depth-doses matched measured values (figures 6–7 and 6–8). The first coupled cavity shift (and hence electric field magnitude in the first half accelerating cavity) was adjusted to optimize both the focal spot size at the target and the target current. The target current is proportional to the x-ray output from the linac. The energy was commissioned by adjusting the power injected into the waveguide through the input port. Figure 6–9 shows the result of the commissioning process for the normalized electron spatial distribution at the target and the normalized energy spectrum. The best match to measurement resulted from a first-coupled cavity shift of 0.25 mm and an input power of 1.3 MW. These parameters resulted in a target current of 136 ± 1 mA,

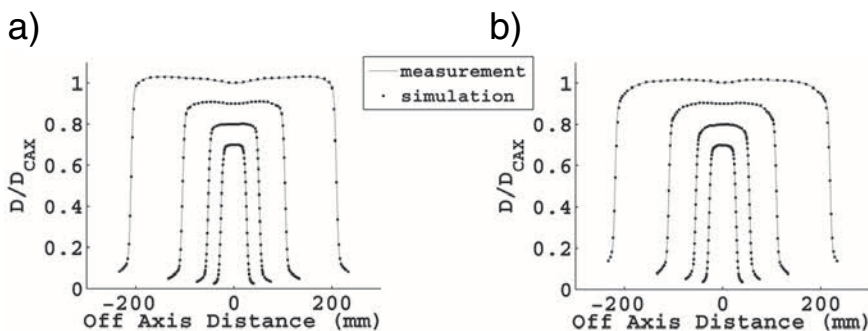


Figure 6–7. a) Crossline profiles for 40×40 , 20×20 , 10×10 , and 5×5 cm² field sizes at 5 cm depth. b) In-line profiles for the same field sizes at a depth of 10 cm. The profiles were initially normalized to the CAX dose and then were scaled in the plots for visual clarity. From (St. Aubin et al. 2010d).

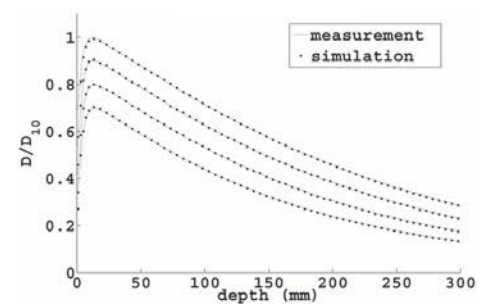


Figure 6–8. The DD curves for the 40×40 , 20×20 , 10×10 , and 5×5 cm² field sizes were initially normalized at D_{10} and were then scaled for visual clarity. The uppermost DD curve is for the 40×40 cm² field, and the bottommost DD curve is for the 5×5 cm² field size, with the 20×20 and 10×10 cm² falling in between. From (St. Aubin et al. 2010d).

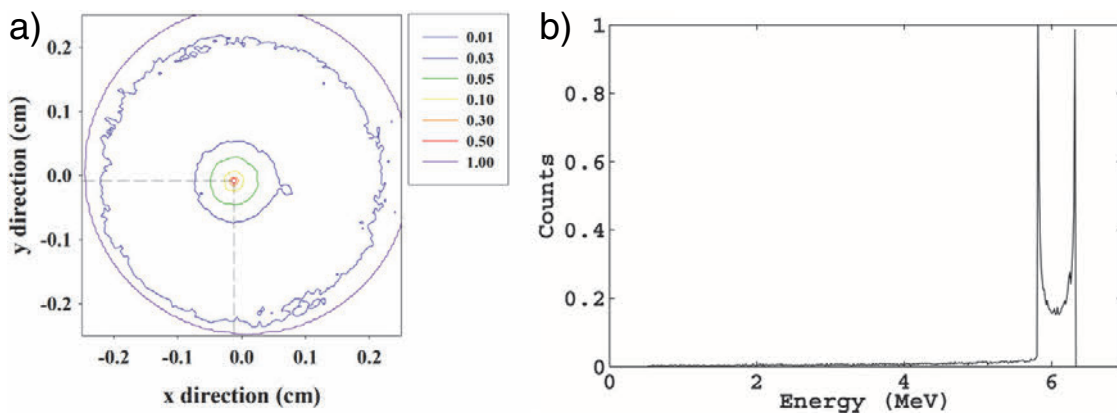


Figure 6-9. a) The normalized spatial intensity distribution at the target, and b) the normalized electron beam energy spectrum for an in-line side-coupled 6 MV linac waveguide. From (St. Aubin et al. 2010d).

which matched measured values on a Varian™ 600C, and a mean energy of 5.6 MeV. A gamma analysis (Low et al. 1998) of the calculated versus measured dosimetric distributions showed that greater than 98% of all points analyzed passed a stringent 1%/1 mm criterion for a $40 \times 40 \text{ cm}^2$ radiation field size, while greater than 99.8% of all points analyzed passed the same criterion for a $5 \times 5 \text{ cm}^2$ field. All points of the simulated depth-dose curves matched measurement to within 1% for depths deeper than 1.5 cm.

6.2.4 Effect of the Magnetic Field on Linac Operation

With the full linac model designed and benchmarked, the operation of a linac in the fringe magnetic fields of a 0.25 T biplanar Alberta linac-MR system was simulated for perpendicular and parallel orientations. As seen for the perpendicular orientation in Figure 6-10, the target current, and hence radiation output, dropped quickly from its nominal value to zero by $1.4 \times 10^{-3} \text{ T}$. As the magnitude of the perpendicular magnetic field increased, the Lorentz force causes the electrons to be deflected farther and

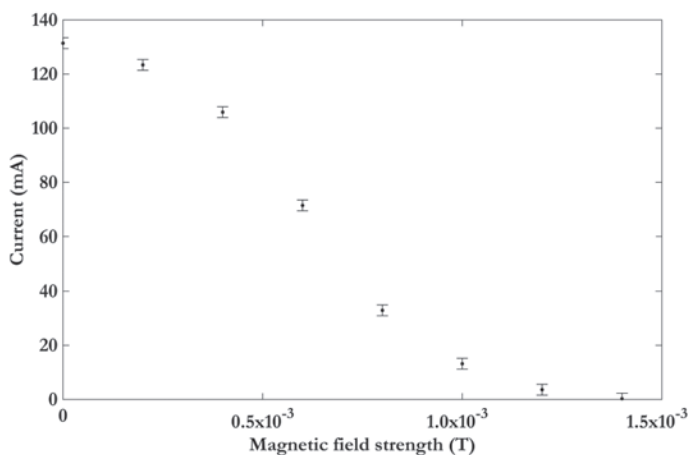


Figure 6-10. The reduction in target current for increasing homogeneous magnetic field strengths is given. At $1.4 \times 10^{-3} \text{ T}$, none of the electrons impact the target. From (St. Aubin et al. 2010c).

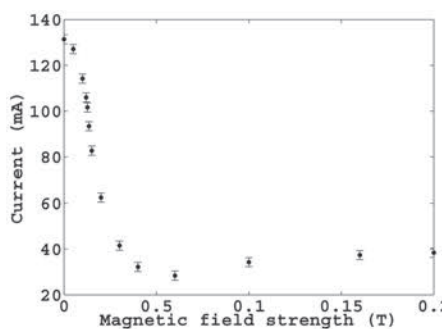
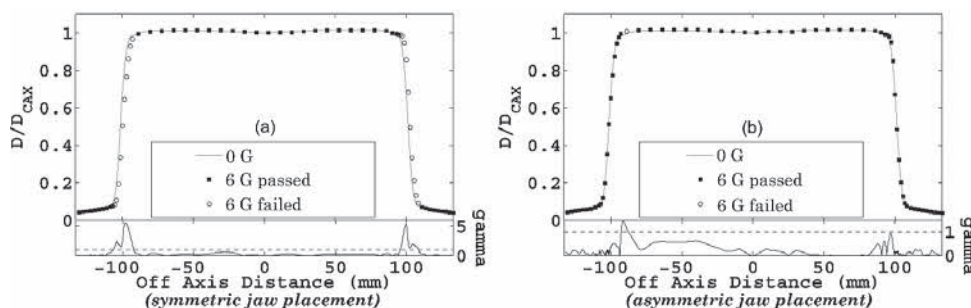


Figure 6-11. Calculated target current with increasing magnetic field strength. The target current decreases, even for increasing injection current up to 0.012 T due to a more non-laminar injected beam. From (St. Aubin et al. 2010b).

Figure 6-11. a) A large lateral shift of the dose profile for the 6 G simulation is seen causing large discrepancies from a typical clinical profile as seen by the gamma index. b) The use of asymmetric y jaw placements almost fully corrects the lateral shift. From (St. Aubin et al. 2010c).



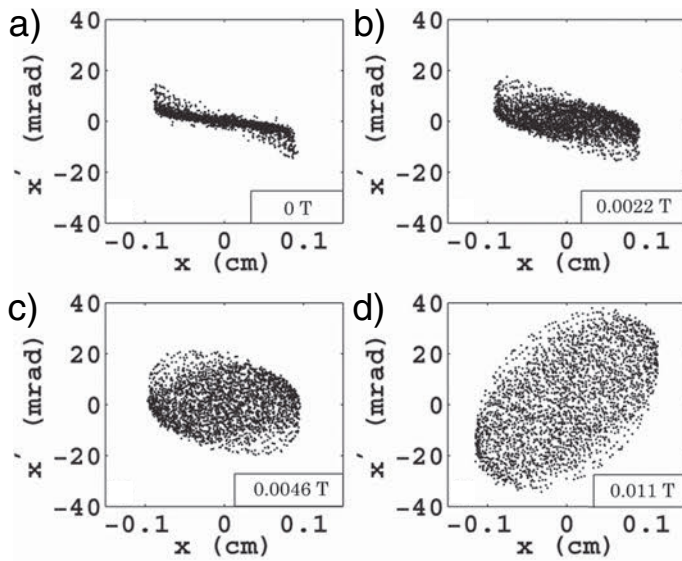


Figure 6–13. The transverse phase space at the exit of the electron gun is given when subjected to a) 0 T, b) 0.0022 T, c) 0.0046 T, and d) 0.011 T parallel magnetic fields. From (St. Aubin et al. 2010b).

farther off-axis. This off-axis deflection caused an asymmetry in the dose profiles, which was calculated to be up to 13% (St. Aubin et al. 2010c). However, if the central axis of the linac waveguide was shifted, compensating for the off-axis shifts of the electron distributions at the target, symmetry could be regained, but at the expense of a lateral shifting of the profile (shown for the 6×10^{-4} T field case in Figure 6–11). However, the lateral shift itself could, in fact, be corrected through the use of asymmetric jaws (Figure 6–11b), but would still have lower x-ray output due to the overall target current loss.

The situation is different for parallel magnetic fields, however, as seen in Figure 6–12, where a minimum target current of around 28 mA was calculated at a magnetic field strength of 0.06 T (St. Aubin et al. 2010b). Magnetic collimation of the accelerating electrons within the waveguide causes the slight increase in target current seen for magnetic field strengths greater than 0.06 T. Despite the fact that the target current never completely decreases to zero, large reductions in target current are still seen. In the parallel orientation, the magnetic field changes the electron optics of the electron gun, resulting in changes to the emittance and radius of the electron beam injected into the linac waveguide. Figure 6–13 shows the evolution of the transverse RMS emittance of the injected beam, beginning from a fairly laminar beam in Figure 6–13a, and transforming into a highly non-laminar beam in Figure 6–13d as the magnetic field strength is increased. This change in injection emittance creates a suboptimal capture condition, reducing the target current. In addition to the emittance changes, the overall beam radius increases as the magnetic field increases, to a point where the beam radius is larger than the injection hole of the

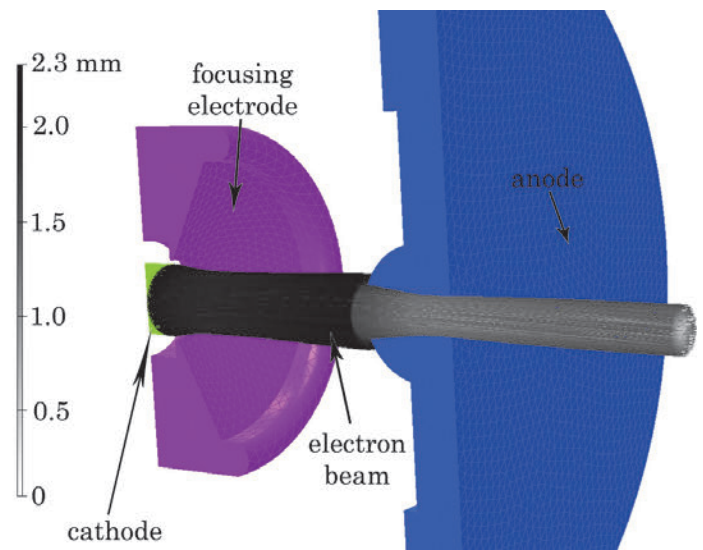


Figure 6–14. The 3D OPERA-3d/SCALA electron gun and trajectory solution in a 0.06 T parallel magnetic field is shown. The structure on the right is the anode, while the structures on the left are the focusing electrode and cathode (mostly hidden behind the electron beam). The electron beam color signifies its radial location in mm. Much of the beam is incident on the anode at 0.06 T. From (St. Aubin et al. 2010b).

waveguide (Figure 6–14). These two factors cause the decreases in target current seen in Figure 6–12.

6.2.5 Magnetic Decoupling of the Linac from the MRI

Methods to mitigate the negative effects of the magnetic field on the linac are required to ensure proper operation for radiotherapy. For the perpendicular configuration, both passive and active shielding were investigated and found to be suitable options to magnetically decouple the MRI from the linac (St. Aubin et al. 2010e; Steciw et al. 2007). An example configuration for passive shielding of the linac is shown in Figure 6–15, where a multi-leaf collimator (MLC) shield was designed to reduce the magnetic field at the MLC to ensure proper operation of the motors (Yun et al. 2010), and a thin submillimeter steel waveguide shield surrounded the linac waveguide and electron gun. Due to the difficulty in reducing the perpendicular magnetic fields to extremely low levels, some residual target current loss is inevitable for passive shielding applications. The MLC passive shield was shown to have a large effect on the MRI homogeneity as well, creating a perturbation of 220 ppm (St. Aubin et al. 2010e). This perturbation was thought to be manageable using standard shimming techniques. However, if non-magnetic MLC motors are employed, no MLC shielding is required, and perturbation of the MRI homogeneity could be reduced to 5 ppm. Optimized active shielding, although more complicated, produced better results, including no calculated target current

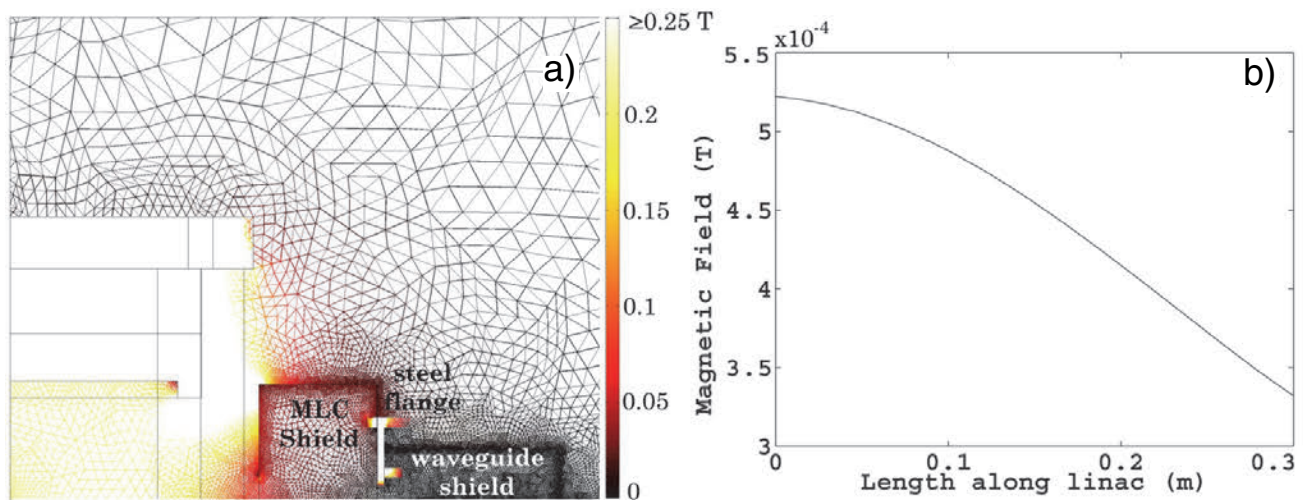


Figure 6–15. a) A 2D field map of the linac-MR system, including the MLC and the linac accelerator waveguide, both residing within their own optimized cylindrical shielding and overlaid on the finite element mesh. The lower left-hand corner is the MR's isocenter, and the top of the figure displays the MR's magnetic fringe fields. b) The linac target is at 0 and the electron gun cathode at 0.3 m. From (St. Aubin et al. 2010e).

loss and only minimal perturbation of the MRI homogeneity of less than 10 ppm (St. Aubin et al. 2010e).

In order to improve the signal-to-noise (SNR) ratio of the MRI images, a new linac-MR system was designed utilizing a 0.5 T superconducting MRI. Magnetic decoupling of the linac from this new MRI was investigated for a parallel configuration (Santos et al. 2012). For passive shielding, submillimeter-thickness steel shielding was required to eliminate any target current losses, and this produced a perturbation of the MRI homogeneity of less than 20 ppm. Active shielding produced better results, again achieving no losses of target current and an MRI homogeneity perturbation of 1 ppm. It should also be noted that the active shielding power and cooling requirements for the parallel configuration was less than for the perpendicular configuration. In addition to magnetic decoupling techniques for the parallel configuration, it was shown by another group (Constantin et al. 2014) that the electron optics of the electron gun could be redesigned to incorporate the effects of a parallel magnetic field.

Through simulation of the linear accelerator and the MRI of a linac-MR system, the effects of magnetic fields on the accelerating electrons can be calculated. This is true for both the perpendicular and parallel magnetic field configurations. While it has been shown that mitigating the negative effects of a perpendicular magnetic field is much more difficult than for a parallel magnetic field, both passive and active magnetic shielding have been successful in magnetically decoupling MRI from the linac in the Alberta linac-MR. Most importantly, tools and processes have been developed that allow the investigation of magnetic field effects of future linac-MR designs.

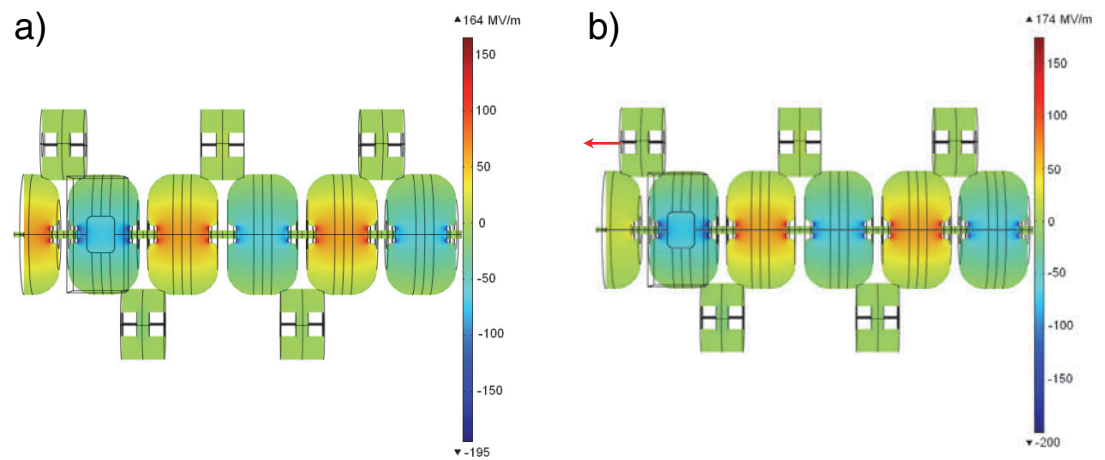
6.2.6 Short 10 MV Linac Development

Although linac-MR devices offer significant improvements over conventional radiotherapy, their ability to deliver optimal dose

distributions is limited due to the present state-of-the-art linac technology. Current linac-MR systems use low-energy linacs. Because of their short length (~30 cm) and simple design, low-energy linacs are relatively easy to magnetically shield and incorporate into a linac-MR system (St. Aubin et al. 2010e; Santos et al. 2012). However, they are restricted to a single 6 MV (Santos et al. 2012) or 8 MV (Crijns et al. 2014) x-ray energy for treatment. In contrast, optimal dose distributions in the clinic are achieved by using high-energy linacs capable of delivering multiple x-ray energies: low energies (6 MV) for more superficial tumors and medium (10 MV) or high energies (15 MV) for deep-seated tumors. High-energy linacs are long (150–250 cm) and complex, requiring buncher cavities for proper electron injection into the linac, focusing coils to prevent electron divergence, and bend magnets to redirect the electron beam onto the target (Karzmark 1993). All of these additional components are affected by stray MR fringe fields, and particularly for bi-planar MRs, the linac's perpendicular orientation and length makes them especially susceptible to Lorentz force effects and difficult to magnetically shield. For these reasons, high-energy linacs have not been incorporated into linac-MR systems, and to date these remain single, low-energy treatment machines.

To address the shortcomings of present linac technology for use in linac-MR systems, a new short-length S-band linac capable of delivering energies up to 10 MV has been designed (Bailie et al. 2015). The RF fields in an eleven-cavity side-coupled linac similar to the Varian 600C linac (Figure 6–5) were 3D-modeled in COMSOL, where instead of being powered by a 2.5 MW magnetron, a 7.5 MW klystron was used. This new linac's cavity dimensions were stochastically optimized to match published Q-factor, shunt impedance, and ratio of peak-to-average electric field values (Tanabe 1983), which are associ-

Figure 6–16. 2D electric field magnitudes from the new linac for a) the unshifted model and b) the 1.45 mm shift, where the direction of the first coupling cavity shift is illustrated by the arrow in b). Note the decreased field magnitudes in the first (leftmost) accelerating cavity after the shift is implemented.



ated with a specific experimentally measured electric breakdown threshold of 239.4 MV/m. The field solutions obtained through COMSOL, together with the electron gun phase-space generated in previous work (St. Aubin et al. 2010c), were used in PARMELA to obtain a phase space of the electrons incident on the linac’s target. As previously discussed, the magnitude of the electric fields in the linac’s first accelerating half-cavity are crucial in determining the electron beam parameters at the target, and these fields were optimized by shifting the first coupling cavity toward the linac gun. Figure 6–16 shows the changes in electric field magnitude in the half-cavity when the first coupling cavity is moved 1.45 mm toward the gun (relative to the mid-position between the first two accelerating cavities); for zero shift the mean magnitude of the electric fields along the central axis is 48.4 MV/m (Figure 6–16a), and with a 1.45 mm shift they are 15.4 MV/m (Figure 6–16b). The effect of altering the fields in the first cavity on the linac’s electron energy spectra at the target can be seen in Figure 6–17 for both shifts, along with the energy spectrum emulating a Varian 10 MV linac (Sheikh-Bagheri et al. 2002). The effects of varying the first

coupling cavity position on the incident electron beam’s FWHM, mean energy, and current are shown in figures 6–18 through 6–20, where the horizontal dotted line shows the values for a Varian 10 MV linac. For a first coupling-cavity shift of 1.45 mm, metrics from the incident electrons at the linac target are very comparable to a Varian 10 MV linac, but are achieved with a total linac length of only 27.5 cm, 5 to 10 times shorter than currently available high-energy linear accelerators. In addition, the maximum electric fields in the new linac are 12% below the experimental breakdown threshold of 239.4 MV/m, therefore no adverse effects of powering the linac with a klystron are expected.

Monte Carlo simulations were conducted to investigate the dosimetric behavior of the x-rays generated from the new short 10 MV linac. The phase space at the target of the 1.45 mm coupling-cavity-shifted linac was generated using PARMELA, and used in a Varian 10 MV treatment head via EGSnc radiation transport codes. The percent depth-dose (PDD) curves for 4×4 , 10×10 , and 20×20 cm² fields in water are shown in Figure 6–21 for the new linac and a simulated Varian 10 MV linac. Regardless of field size, the new linac PDDs are nearly identical to the Varian 10 MV PDDs. Analysis of the penumbra from a 10×10 cm² field reveals that the new 10 MV linac has a smaller penumbra (5.0 mm) compared to the penumbra Varian 10 MV linac (5.6 mm), as seen in Figure 6–22.

In order to address the need for lower energies, the successful implementation of variable energy switches (Karzmark 1993) has recently been incorporated into the new 10 MV linac. In addition to 10 MV x-rays, these switches give the new linac the ability to generate multiple lower x-ray energies as well (8 MV, 6 MV, etc). With the addition of multiple energies, the development of the short 10 MV linac will fill the technological void needed to fully optimize linac-MR systems. With this new linac, the optimal x-ray energy can be selected on a beam-by-beam basis, allowing linac-MR systems to fully optimize their treatment deliveries, as is done on all modern treatment machines. With the increased dose rate, sharper penumbra, and

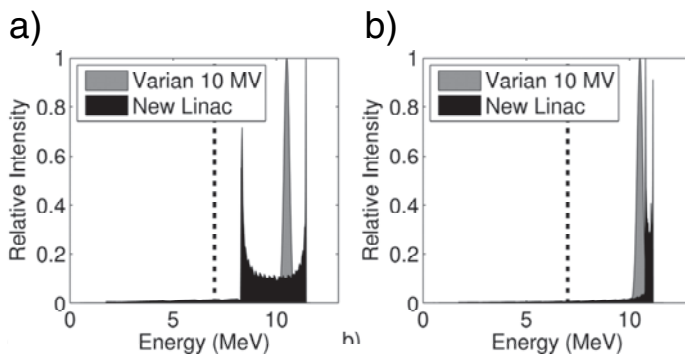


Figure 6–17. Electron energy spectrum produced by an emulated Varian 10 MV linac (gray) compared to the spectrum produced by the new linac design (black) for the unshifted model a) and the 1.45mm shift b). The dashed line is the 7 MeV cutoff, below which electrons were not included in the beam energy or beam current calculations. From (Baillie et al. 2015).

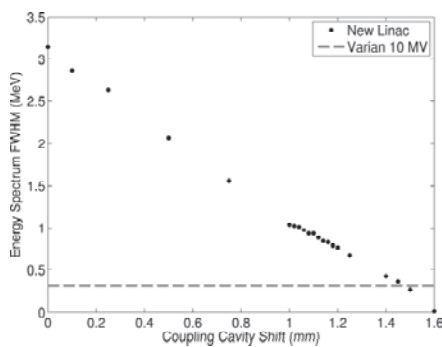


Figure 6–18. Electron beam FWHM as the coupling cavity is shifted (black points), compared with that of the spectrum of an emulated Varian 10 MV linac (dashed gray line). From (Baillie et al. 2015).

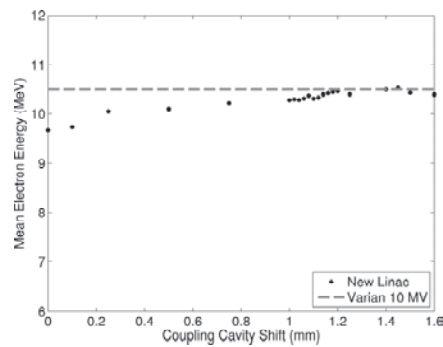


Figure 6–19. Electron beam energy as the coupling cavity is shifted (black points), compared with that of an emulated Varian 10 MV linac (dashed gray line). Electron beam energy is defined here as the mean energy of the electrons with energies greater than 7 MeV. From (Baillie et al. 2015).

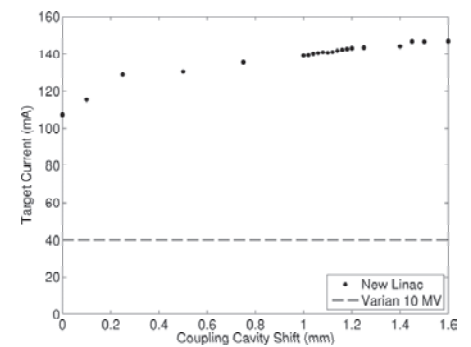


Figure 6–20. Waveguide target current as the coupling cavity is shifted (black points) compared against the target current measured on a Varian 10 MV linac (dashed gray line). The target current only includes those electrons with energies greater than 7 MeV. From (Baillie et al. 2015).

the improved dose distributions achievable by the new linac, we expect it to be a valuable tool for future linac-MR systems.

6.2.7 Linear Accelerator Effects on MRI RF Coils

Integrating a linear accelerator with an MRI system exposes the MRI RF coils to both the radiofrequency (RF) noise and the pulsed radiation of the linac. Both of these can have deleterious effects on MRI image quality and, therefore, interfere with accurate image guidance.

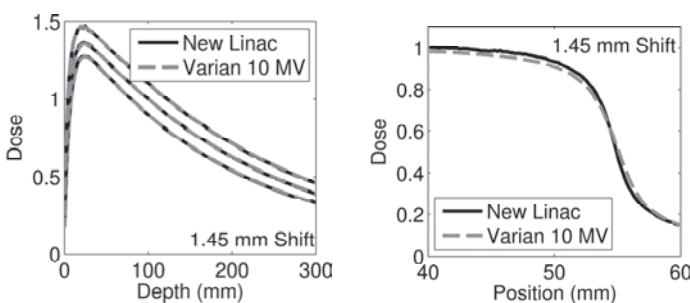


Figure 6–21. Depth-dose profile from an emulated Varian 10 MV linac (dashed gray) compared to the profile produced by the new linac design (solid black) for the 1.45 mm cavity shift. Each field size has been normalized at 10 cm depth, and then independently scaled for clarity (scaling factors of 0.9, 1.0, and 1.1 for field sizes of 4 x 4, 10 x 10, and 20 x 20 cm², respectively). From (Baillie et al. 2015).

Figure 6–22. Beam penumbra from an emulated Varian 10 MV linac (dashed gray) compared to the penumbra produced by the new linac design (solid black) for the 1.45 mm cavity shift. Each field is normalized to the central axis dose. From (Baillie et al. 2015).

RF noise and shielding

The RF noise emitted by a clinical linear accelerator was measured and characterized for the first time by Burke et al. (2009). Their work showed that magnetron-based linacs emit RF noise on the order of tens of μWm^{-2} , while klystron-based linacs emit RF noise on the order of μWm^{-2} , both in the frequency range used by MRI RF coils (Burke et al 2009). The RF power received by RF coils is also on the order of μW , so the RF noise could interfere with image acquisition by providing extraneous signal to the coils. Using the linac-MR prototype described by Fallone et al., the RF shielding and the feasibility of imaging during the pulsing of a clinical linac was evaluated by Lamey et al. (2010). Their work shows that extreme care must be used in designing the RF cage to shield from magnetron-emitted RF, and all seams must be carefully sealed with copper tape, etc. They also note that all cables fed into the RF cage required shielding and filtering to avoid transmission of the RF noise into the RF cage. The effect of insufficient RF shielding on MR images was shown to be a degrading of imaging SNR when images were acquired with the linac producing pulsed radiation compared to images acquired with no linac pulsing (Fallone et al. 2009; Lamey et al. 2010). In their work, the radiation was blocked by a lead shield before reaching the coil to isolate RF effects (Lamey et al. 2010). When proper RF shielding was used there was no difference in SNR for MR images acquired with and without the linac producing pulsed radiation.

Radiation-induced current

When high-energy (MeV) photons strike thin metals, e.g., the copper windings used as the conductors in MRI RF coils, high-energy Compton electrons are produced and ejected from the conductor. This efflux of electrons produces a charge imbalance in the conductor, and it becomes positively charged. If the metal conductor is part of an electrical circuit, e.g., RF coils, electrons

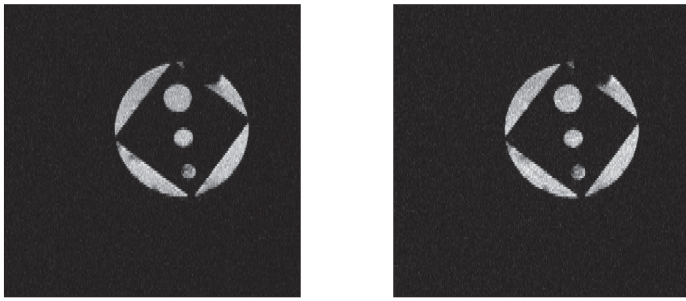


Figure 6–23. Sample images acquired with 3 cm solenoid coil. The images were acquired with the linac not producing radiation (left) and with linac producing radiation and RF coil unblocked at 250 MU/min (right). The RIC artifact is not visible. Taken from (Burke et al. 2012a).

flow from the circuit into the coil to neutralize the charge imbalance. This leads to a current from the coil into the circuit, known as radiation-induced current (RIC); it is also called Compton current because it is produced via Compton scattering and has been reported on in various systems by several authors (Meyer et al. 1956; Johns et al. 1958; Degenhart et al. 1961; Abdel-Rahman et al. 2006).

Burke et al. (2010) showed that pulsed radiation produced a measurable RIC in an RF coil using a series of measurements with an RF coil inside an RF cage irradiated by a linear accelerator. These measurements suggested electronic disequilibrium in the RF coil windings as the source of RIC, as the addition of

wax buildup was able to reduce the measured RIC. The use of the RF cage was necessary because of the RF noise discussed in Section 6.2.7.

The effect of RIC on images acquired with an integrated linear accelerator/magnetic resonance imager (linac-MR) was evaluated using the system designed and built by Fallon et al. (2009). The presence of RIC in the received signal, due to the pulsed radiation incident on the RF coil, reduced the SNR in images compared to images acquired with no radiation incident on the coil (Burke et al. 2012a; Burke et al. 2012b). Figure 6–23 shows that the decrease in SNR is not always visually obvious in the final image, but a closer examination of the raw k -space data shows the presence of RIC, visible as lines in Figure 6–24. In order to isolate the source of the k -space lines as RIC and not RF noise from the linear accelerator, the “no-radiation” images were acquired with the linear accelerator producing radiation but the radiation beam intercepted and absorbed by a lead block before reaching the RF coil. The residual RF noise, if present, would still reach the coil even if the x-ray beam was completely attenuated by the lead block. The lack of lines in the “no radia-

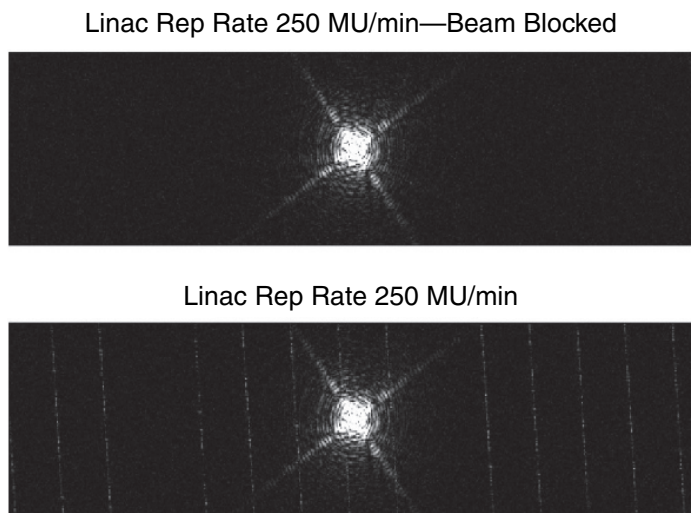


Figure 6–24. k -space data from images acquired with linac dose rates of 0 and 250 MU/min. The top image was acquired with a linac dose rate of 250 MU/min, but the radiation beam was blocked from reaching the coil; it shows no RIC effects. The bottom image was acquired with a linac dose rate of 250 MU/min and the radiation beam incident on the RF coil; it clearly shows the RIC artifact, which presents itself as near vertical lines in k -space. Taken from (Burke et al. 2012a).

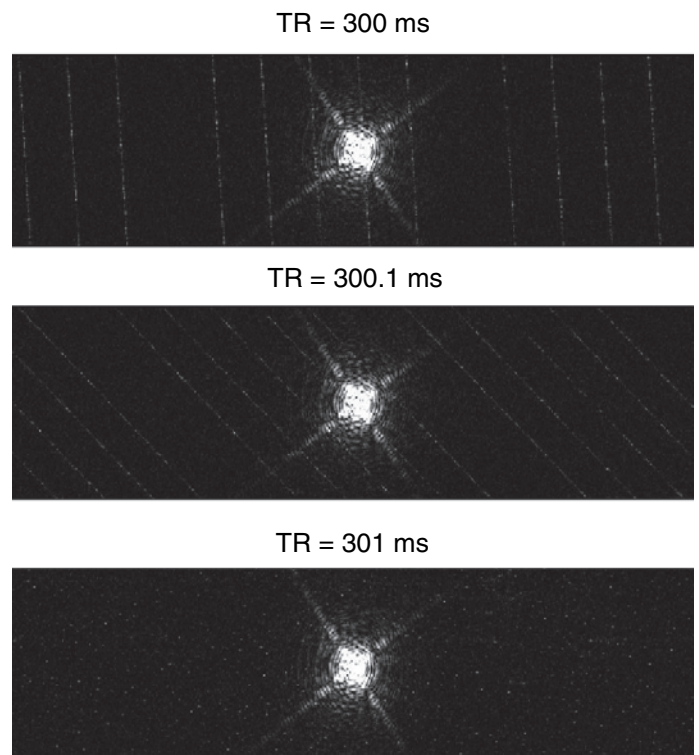


Figure 6–25. k -space data for gradient echo images acquired with a linac dose rate of 250 MU/min and the radiation beam incident on the RF coil. Top image: TR = 300 ms; middle image: TR = 300.1 ms; bottom image: TR = 301 ms. Images show the interplay between linac pulsing and MR sequence timing. The RIC pulses on each line horizontal k -space line are equally spaced, based on the linac pulse rate, but the relative position of the RIC pulses on subsequent k -space lines is dependent on MR sequence timing. Taken from (Burke et al. 2012b).

tion” k -space data (Figure 6–24) shows the absence of both RIC and RF noise.

The appearance of the RIC artifact as lines in k -space is a consequence of the timing of the imaging sequence. If the MR imaging parameter TR (repetition time) is changed even slightly, the appearance of the RIC can change drastically as shown in Figure 6–25, which shows images of the k -space data for TR values of 300 ms, 300.1 ms, and 301 ms. A small change, 0.1 or 0.2 ms, in TR results in a large change in the k -space distribution of the RIC artifact. If the TR is changed from 300 to 300.1 ms, the slope of the lines seen in k -space changes dramatically, and more lines are seen; 12 lines are seen with TR = 300 ms, while 14 are seen with TR = 300.1 ms. When the TR is changed by larger amounts (i.e., 1 ms and up) the RIC appears as random background spikes, seen in the bottom image of Figure 6–25 (TR = 301 ms). A closer inspection shows that the random spikes are still regularly spaced on each read encode line (horizontal line). Aside from the SNR loss, the various k -space artifact patterns had no discernible effects in image space. The regular spacing of k -space spikes due to RIC is explained by examining the timing between the linear accelerator and the imaging sequence.

The linear accelerator pulses with a frequency of 180 Hz, leading to 1 radiation pulse every ~5.6 ms. Examining the original imaging sequence with a TR of 300 ms, a simple calculation reveals 54 radiation pulses per TR ($300 \text{ ms} \times 180 \text{ pulses/s}$)—not all of these are seen in k -space because the actual acquisition time for the MR sequence is much shorter than the total TR, and not every linac pulse produces radiation. This exact integer multiple means that the radiation pulses will occur at approximately the same sampling points along a given read encode k -space line (read encode lines are horizontal lines in k -space that are acquired during a single TR), resulting in a near-vertical line in k -space (top image Figure 6–21). Changing TR even by a small amount, such as 0.1 ms to 300.1 ms, means that the number of radiation pulses per TR is no longer an exact integer multiple ($300.1 \text{ ms} \times 180 \text{ Hz} = 54.02$) so the radiation pulses will shift along the read direction resulting, in this case, a line sloping downward from left to right (middle image Figure 6–21). When TR is changed by a larger amount, for example to 301 ms (54.2 pulses per TR), the shift in location of RIC spikes between subsequent read encode lines becomes so large that the noise appears random (bottom image Figure 6–21), though on closer examination the noise spikes due to RIC are still spaced the same distance apart on each read encode line of k -space—as is expected because the linac is still pulsing at 180 Hz.

The loss of SNR was shown to increase as the dose rate of the linear accelerator was increased since more linac pulses now produce radiation, resulting in more lines in k -space (Burke et al. 2012b). The prototype system had a maximum repetition rate of 250 monitor units per minute (MU/min), but most clinical linear accelerators have repetition rates of 600 MU/min or more, so they could suffer even greater SNR loss.

Two methods were devised to reduce or eliminate the SNR loss due to RIC. The first method, described in Burke et al. (2012a), reduces the effect of RIC through the application of buildup material to the RF coil conductive windings in order to attempt to restore electronic equilibrium in the conductors. This method was shown to reclaim up to ~55% of the lost SNR (Burke et al. 2012a), but the presence of extra material in the radiation beam path could have adverse effects on dosimetry, specifically the patient skin dose. This potential dosimetric effect, coupled with only regaining approximately half of the lost SNR, led to the development of the second method of RIC noise reduction. This method is a post-processing tool that removes the RIC artifact from the image k -space data and restores some of the SNR lost due to RIC.

In the post-processing RIC noise reduction approach, software searches pixel by pixel for anomalous signal spikes in k -space and then removes them (Burke et al. 2012b). These spikes are found by searching the k -space data for pixels with intensities above a threshold value representing the average background plus three standard deviations. Once an anomalous pixel is found, its magnitude is then compared to the mean magnitude of the pixels surrounding it to determine whether it resides in a background region (i.e., toward the edges of k -space) or in a signal region (near the center of k -space). If the algorithm determines that the anomalous pixel is in a background region, the pixel value is changed to that of the average background. If the algorithm instead determines that the anomalous pixel is in a signal region, then no action is taken. The algorithm will not eliminate all RIC spikes from the k -space data, as it will not be able to discern between an RIC signal and the MR signal near the center of k -space. However, any RIC spikes near the center of k -space have a minimal effect on SNR because the spikes are sparsely distributed compared to the MR signal. The MR image is then reconstructed from the processed k -space data. The SNR from the processed image is then compared to the original image. Approximately 82% of the lost SNR at 250 MU/min was recovered, yielding an SNR that is 98% of the SNR with no radiation striking the coil. This method shows that RIC can be effectively filtered from the MR signal to provide images with essentially unchanged SNR (Burke et al. 2012b).

6.3 Radiation Dosimetry in Magnetic Fields

The effectiveness of radiation therapy lies in the ability to deposit enough energy in malignant or benign tumors to cause cellular reproductive death. Kinetic energy from secondary electrons set in motion within the body is transferred to the cells, causing DNA damage. In the strong magnetic fields of a linac-MR system, the trajectories of the secondary electrons will be altered by the Lorentz force, resulting in geometric changes to the patterns of dose deposition. Therefore, linac-MR systems require a method of accurately calculating absorbed dose in the presence of the strong magnetic fields of the MRI. In the longitudinal (parallel) rotating bi-planar (LRBP) linac-MR configura-

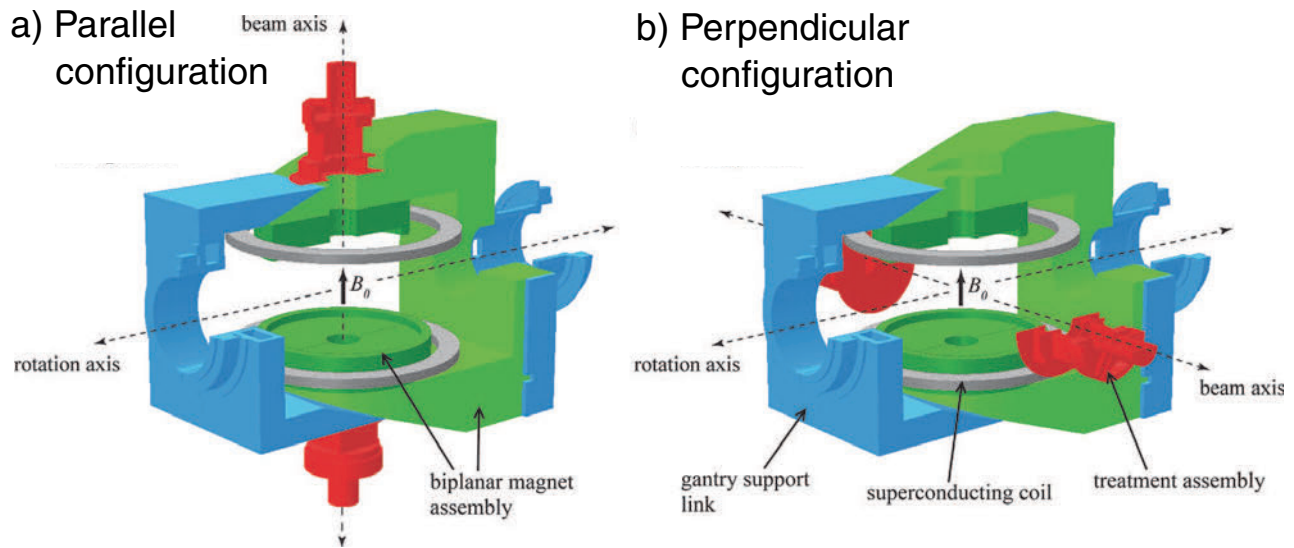


Figure 6–26. Partial sections of the three-dimensional RBP linac-MRI geometries illustrating a) parallel (longitudinal) and b) perpendicular (transverse) configurations showing the orientation of the MRI magnetic field with respect to the radiation beam. From (Keyvanloo et al. 2012).

tion, the MR magnetic field is in-line to the incident photon beam, whereas in the transverse (perpendicular) rotating biplanar (TRBP) configuration, the magnetic field is perpendicular to the photon beam (Figure 6–26). The difference in the orientation of the MRI magnetic field results in different dosimetric effects on the dose distribution inside the patient and on the patient’s surface for the two configurations.

Radiation transport is governed by the linear Boltzmann transport equation (LBTE), which is an integro-partial differential equation that is difficult to solve. The most common methods used in the radiotherapy community to calculate dose distributions are approximate solutions to the LBTE, typically model-based algorithms using the principles of convolution-superposition. These approximate methods have not been shown

to be capable of including the effects of the Lorentz force on the secondary electrons. However, there are two classes of techniques that can solve the LBTE under this scenario: indirect Monte Carlo methods that are stochastic in nature, and direct deterministic methods. Historically, all dose calculations within magnetic fields were performed via Monte Carlo, as seen in sections 6.3.1 and 6.3.2. However, St. Aubin et al. (2015) have recently developed a novel deterministic dose calculation in magnetic fields, as described in section 6.3.3.

6.3.1 In-patient Dosimetry

In linac-MR systems with transverse geometry, the effects of the magnetic field may manifest as changes to percentage depth-doses, lateral shifts in dose distributions, and electron return

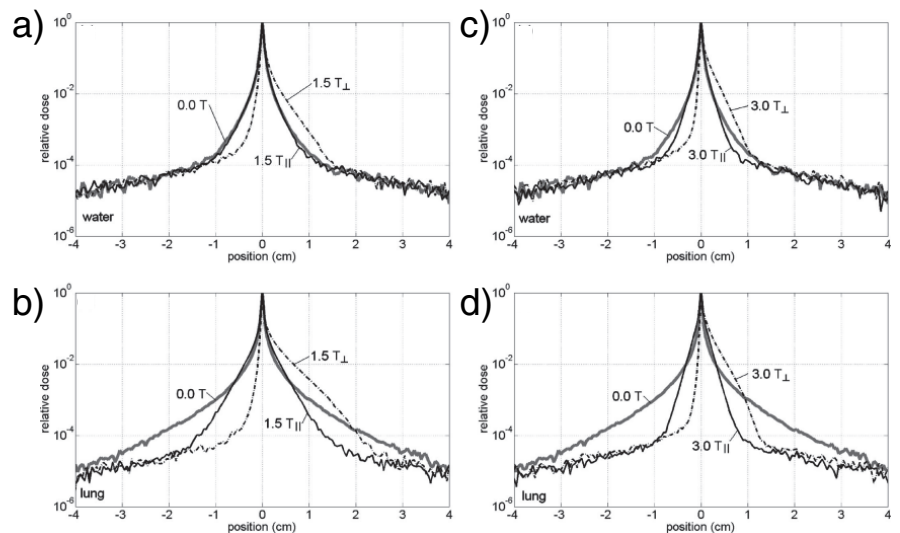


Figure 6–27. The 6 MV pencil beam dose profiles at a depth of 10 cm for field strengths of 1.5 T in a) water and b) lung and 3.0 T in c) water and d) lung. The longitudinal field (indicated by the subscript “||”) confines the distribution radially, while the transverse field (indicated by the subscript “⊥”) shifts the dose distribution to one side. The simulations were performed using the EGSnrc Monte Carlo radiation transport codes. From (Kirkby et al. 2010).

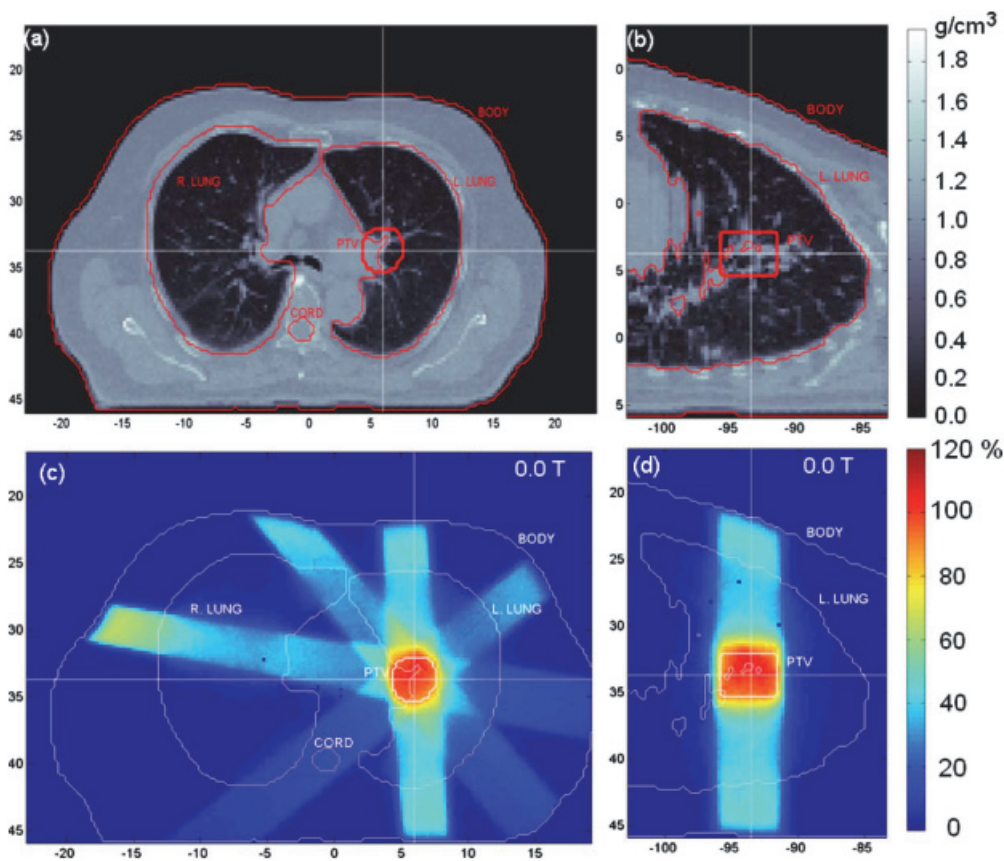


Figure 6–28. Physical density maps in axial (a) and sagittal (b) planes through the isocenter, illustrating the variation in density through the anatomy under examination. Structures are superimposed. Also shown are the dose maps, (c) axial and (d) sagittal, normalized to 100% at the isocenter, for the five-field plan with zero magnetic field strength. From (Kirkby et al. 2010).

effects (EREs) that increase exit dose and cause cold and hot spots at lung/tissue interfaces (Raaijmakers et al. 2004; Raaijmakers et al. 2005; Raaijmakers et al. 2008; Kirkby et al. 2008; Kirkby et al. 2010). These effects are potentially clinically significant, particularly when higher magnetic field strengths are used. With a longitudinal geometry, many of these dosimetric issues within the patient are reduced or eliminated. For example, in contrast to the undesired lateral shift in dose distribution seen in the transverse geometry, the Lorentz force restricts the radial spread of secondary electrons in the patient when the B-field is parallel to the photon beam axis (Bielajew 1993; Chen et al. 2005). This confinement results in a reduced beam penumbra when using a parallel magnetic field (Bielajew 1993; Litzenberg 2001). Kirkby et al. (2010) provided a detailed investigation of dosimetric effects in the presence of both parallel and perpendicular magnetic fields for geometries that include low-density tissue, where the effects will be exacerbated. The study was performed using EGSnrc Monte Carlo radiation transport codes with algorithms implemented to account for the magnetic field deflection of charged particles. The responses to a 6 MV pencil photon beam incident on water and lung slabs for 1.5 and 3.0 T magnetic fields are shown in Figure 6–27. In water, a longitudinal 1.5 T field produces little change to the width of the dose kernel, while at 3.0 T a relatively small, but noticeable restriction of secondary electrons is apparent. However, in lung, a lon-

gitudinal magnetic field produces a sizable reduction in the width of the dose kernel at both field strengths. For the transverse geometry, the magnetic field produces an asymmetric dose response due to the lateral movement of the electrons caused by the Lorentz force; as expected, the effect is also more pronounced in the low-density lung tissue.

To investigate the potential clinical significance of perturbations caused by the magnetic field, Kirkby et al. (2010) also simulated a five-field lung plan in the longitudinal and transverse geometries for magnetic field strengths ranging from 0.2 to 1.5 T. The traditional scenario with no magnetic field is illustrated in Figure 6–28, which shows the variations in physical density in the patient anatomy, and dose maps in the transverse and sagittal planes for the zero magnetic field case. Difference maps relative to this 0 T dose distribution for both RBP transverse and longitudinal linac-MR systems are shown in figures 6–29 to 6–31 for magnetic field strengths of 0.2, 0.5, and 1.5 T, respectively. For the 1.5 T case, in addition to the rotating biplanar transverse geometry, results are also presented for a fixed cylindrical (FC) transverse geometry (see Kirkby et al. 2008), where the magnetic field remains stationary along the cranial-caudal axis (into the page) for all incident beam directions. For the transverse field geometry, the movement of electrons toward the patient's inferior results in differences of up to $\pm 12\%$ in the lung tissue at 0.2 T, and up to $\pm 20\%$ at 0.5 T. Tissue interface

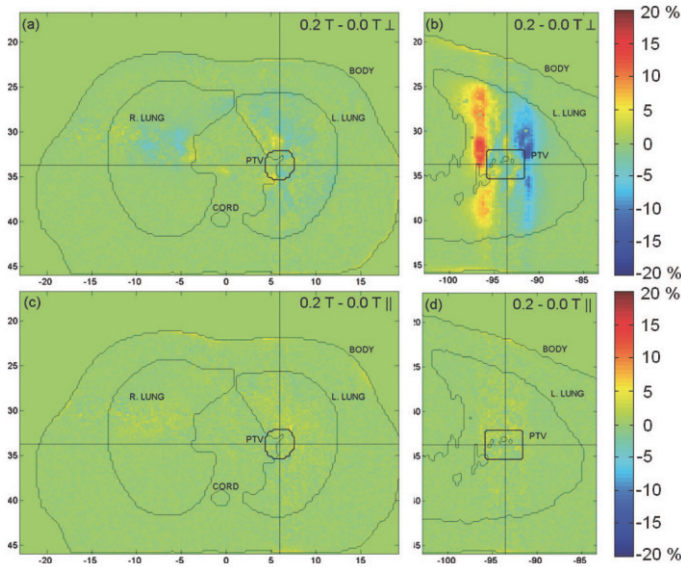


Figure 6–29. Relative dose differences for a lung five-field plan at a magnetic field strength of 0.2 T in (a)–(b) the transverse geometry and (c)–(d) the longitudinal geometry. Differences of $\pm 12\%$ are seen in the lung in the transverse geometry. In the longitudinal geometry, differences from the zero field case are minimal. The simulations were performed using the EGSnc Monte Carlo radiation transport codes. From (Kirkby et al. 2010).

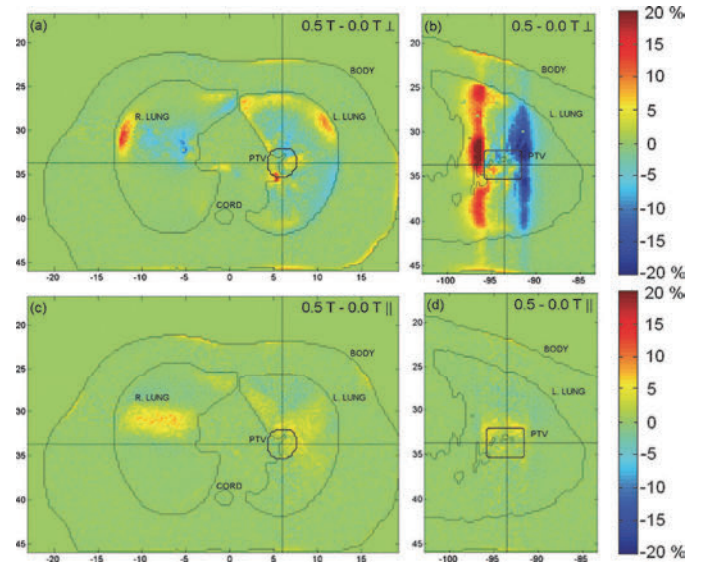
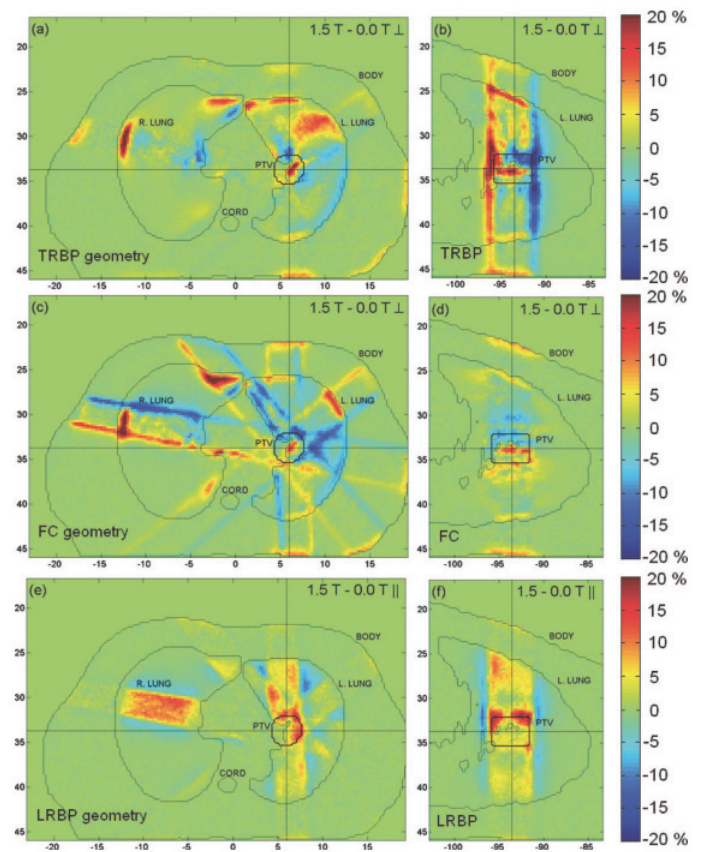


Figure 6–30. Relative dose differences for a lung five-field plan at a magnetic field strength of 0.5 T in (a)–(b) the transverse geometry and (c)–(d) the longitudinal geometry. Lung/tissue interface effects (ERE) manifest in the transverse geometry, and a dose shift inside the lungs results in extreme dose differences of 20%. In the longitudinal geometry, differences from the zero field case are less than 5%. The simulations were performed using the EGSnc Monte Carlo radiation transport codes. From (Kirkby et al. 2010).

Figure 6–31. Relative dose differences for the lung five-field plan at 1.5 T. (a)–(b) show the TRBP geometry, where the magnetic field changes with beam direction. In (c)–(d), results are also shown for the fixed cylindrical (transverse) geometry, where the magnetic field is static in the cranio-caudal direction. In both transverse geometries, the tissue interface effects are apparent. In the LRPB geometry, (e)–(f), dose increases of up to 15% are observed inside the primary photon beam in the lung tissue, while dose differences in soft tissue outside of the lung remain minimal. The simulations were performed using the EGSnc Monte Carlo radiation transport codes. From (Kirkby et al. 2010).



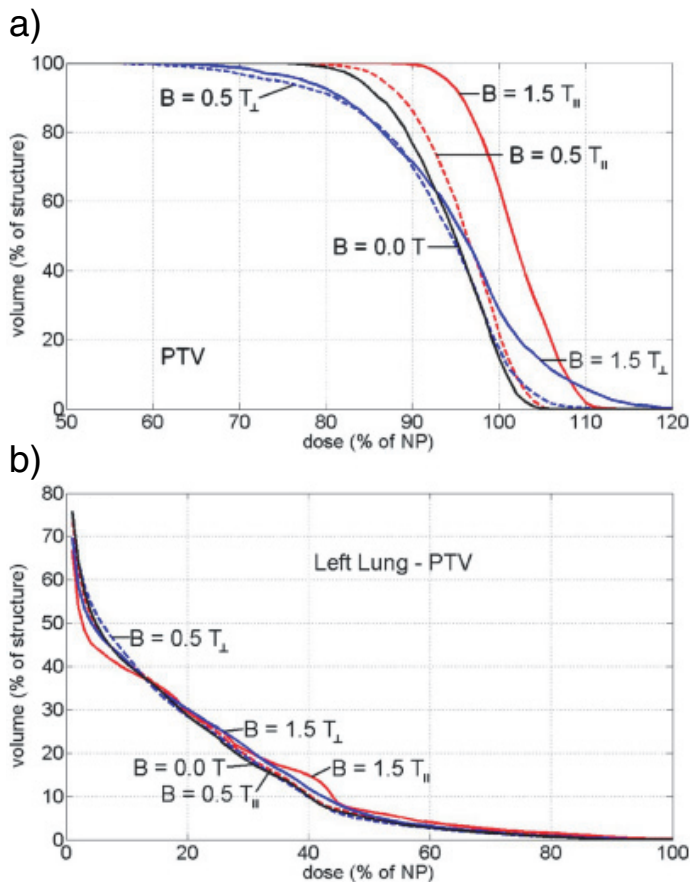


Figure 6-32. Dose volume histogram for a) the PTV and b) the left lung considering magnetic field strengths of 0.0, 0.5, and 1.5 T. The simulations were performed using the EGSnrc Monte Carlo radiation transport codes. From (Kirkby et al. 2010).

effects, while minimal at the lowest field strength, become apparent at 0.5 T. At 1.5 T the interface effects result in dose differences as high as 30% for either the TRBP or FC geometry. For the LRBP geometry, changes to the in-patient dose distribution are much smaller in magnitude. Differences from the zero field case are minimal throughout the patient volume at 0.2 T and remain below approximately 5% at 0.5 T. At 1.5 T, dose differences of up to 15% are seen; however, hot spots are confined to the volume irradiated by the primary photon beams and volumes outside these regions are noticeably colder.

The cumulative impact of the magnetic field dose effects are represented in the cumulative dose-volume histograms (DVHs) shown in Figure 6-32. In the longitudinal geometry, the DVH of the planning target volume (PTV) shifts increasingly to the right at larger field strengths, reflecting a desirable increase in dose to the target volume. The shift can be attributed to a reduction in the lateral range of electrons, resulting in more dose remaining within the PTV; since in this plan the PTV includes a significant amount of lower density lung tissue, the shift in the DVH is appreciable. For the transverse geometry, the PTV dose distribution undesirably becomes more heterogeneous as the

magnetic field increases, as evident from the longer tails and larger shoulders in the DVH. The DVH for the left lung (with PTV excluded) shows that the cumulative dose differences are relatively small with respect to the zero field case at 0.5 and 1.5 T field strengths in both configurations. Although figures 6-30 and 6-31 show obvious changes in the local dose distribution within the lung, the effect of the magnetic field is primarily to shift the dose within the lung. Regions within the lung become hotter and some colder, but in general, the integral dose remains relatively constant. Considering the impact on both PTV and lung DVHs, in the longitudinal geometry, increasing field strength may allow a reduction in integral lung dose for a given PTV dose in comparison to the conventional 0 T treatment. In contrast, in the transverse geometry, integral lung dose may need to increase to achieve an acceptable level of dose coverage of the PTV, owing to the broader PTV shoulder.

6.3.2 Surface Dose

Changes to patient skin dose are another important consideration for linac-MR systems. Contaminant electrons that reach the patient surface are the main contribution to skin dose at the beam entrance in megavoltage photon beams. These electrons are produced by interaction of the photon beam with various components in the head of the linear accelerator. The magnetic field of the MRI unit perturbs the fluence of these electrons and, hence, alters the skin dose in both linac-MR configurations. In a transverse system (TRBP or FC), a reduction in skin dose is expected, since the contaminants may be swept away from the incident path of the x-ray beam. Entrance and exit doses have been studied extensively for the FC geometry by Raaijmakers et al. 2007, Oborn et al. 2009, and Oborn et al. 2010, and in TRBP and LRBP linac-MR systems (specifically, our V.1 of Figure 6-3) by Keyvanloo et al. (2012). In a TRBP linac-MR system, on the entry side, the central axis skin dose is less than that for the zero magnetic field case for small surface angles, but increases strongly for large angles (Figure 6-33). The changes in the entrance skin dose due to the magnetic field also depend on the field size of the incident photon beam: the reduction in entrance dose along the central axis increases as field size is increased (Figure 6-33b). On the exit side of an FC or TRBP linac-MR system, the surface dose is significantly increased due to the electron return effect, as illustrated by the PDD in Figure 6-34. The increase in the exit dose is dependent on both the exit surface orientation and the field size (Figure 6-35).

In the LRBP linac-MR configuration, the exit dose does not increase since electrons do not return back to the surface once they exit the patient. However, lateral confinement of contaminant electrons results in increased entrance dose within the area of the beam since electrons that would be scattered away from the patient when there is no magnetic field are directed to the patient surface by a longitudinal field. However, the increase in entrance dose for the LRBP linac-MR configuration is generally small compared to the dose at d_{max} ; its magnitude depends

on the size of the air gap between the patient top and the magnet pole and on the field size of the incident beam (Figure 6–36), approaching zero for small air gaps and large field sizes.

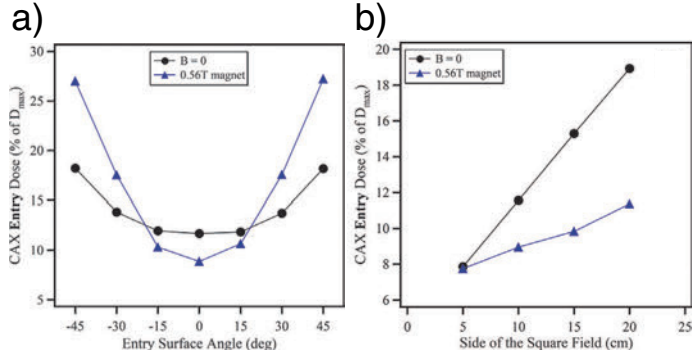


Figure 6–33. The central axis entry skin dose of the transverse linac-MR system as a function of a) the surface angle and b) the field size in the presence of the 3D magnetic field of a 0.56 T MRI. The simulations were performed using the EGSnrc Monte Carlo radiation transport codes. From (Keyvanloo et al. 2012).

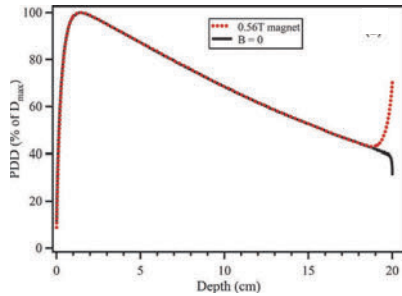


Figure 6–34. The central axis percent depth-dose (PDD) of the RBP transverse linac-MR system in the presence of the 3D magnetic field of a 0.56 T MRI showing the effect of the ERE on the exit side. The simulations were performed using the EGSnrc Monte Carlo radiation transport codes. From (Keyvanloo et al. 2012).

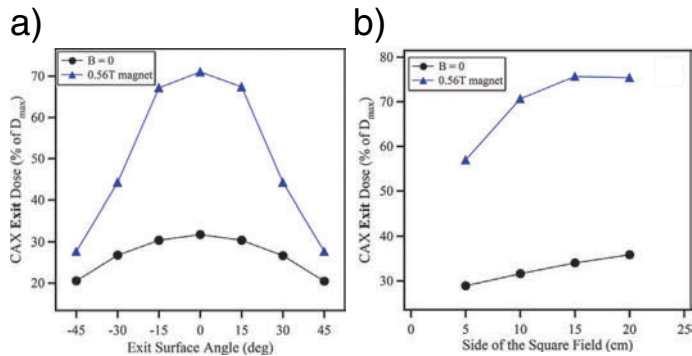


Figure 6–35. The central axis exit skin dose of the transverse linac-MR system as a function of a) the surface angle and b) the field size in the presence of the 3D magnetic field of a 0.56 T MRI. The simulations were performed using the EGSnrc Monte Carlo radiation transport codes. From (Keyvanloo et al. 2012).

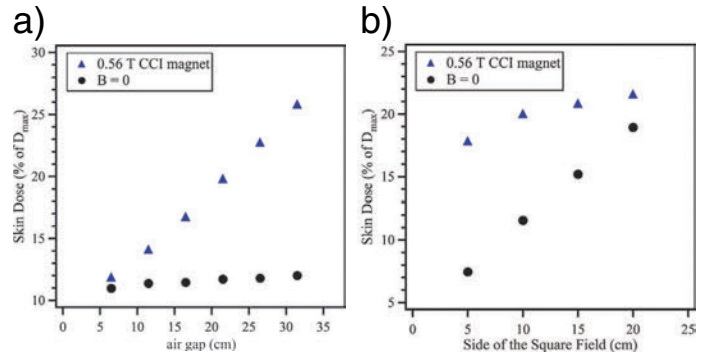


Figure 6–36. The central axis entry skin dose of the longitudinal linac-MR system as a function of a) the air gap between the patient top and the magnet pole and b) the field size in the presence of the 3D magnetic field of a 0.56 T MRI. The simulations were performed using the EGSnrc Monte Carlo radiation transport codes. From (Keyvanloo et al. 2012).

6.3.3 Deterministic Dose Calculations in Magnetic Fields

The continuous slowing down approximation LBTE used for electron calculations can be expressed as

$$\begin{aligned} \vec{\Omega} \cdot \nabla \psi(\vec{r}, E, \vec{\Omega}) + \sigma \psi(\vec{r}, E, \vec{\Omega}) \\ - \frac{\partial}{\partial E} (\beta_r(\vec{r}, E) \psi(\vec{r}, E, \vec{\Omega})) - Q^{xy}(\vec{r}, E, \vec{\Omega}) = S(\vec{r}, E, \vec{\Omega}) \end{aligned} \quad (6.1a)$$

with

$$Q^{xy}(\vec{r}, E, \vec{\Omega}) = \int_{\Omega} d\vec{\Omega}' \int_0^{\infty} dE' \sigma_s^{xy}(\vec{r}, E' \rightarrow E, \vec{\Omega} \cdot \vec{\Omega}') \psi_x(\vec{r}, E', \vec{\Omega}') \quad (6.1b)$$

and

$$\vec{\Omega} = \frac{\vec{v}}{v} = (\sin \theta \cos \phi, \sin \theta \sin \phi, \cos \theta) \quad (6.1c)$$

In Equation 6.1, E is the particle kinetic energy, \vec{v} is its velocity, σ is the macroscopic total cross section (absorption and scattering), σ_s is the macroscopic differential cross section, β_r is the restricted mass stopping power, S is the source, ψ is the angular fluence, and (θ, ϕ) are spherical polar and azimuthal angles. The superscript notation in Equation (6.1b) denotes particle x creating secondary particle y , and the integration is over the surface of the unit sphere.

As shown (St. Aubin et al. 2015), a force term can be added to Equation (6.1) as follows

$$\begin{aligned} \vec{\Omega} \cdot \nabla \psi(\vec{r}, E, \vec{\Omega}) + \sigma(\vec{r}, E) \psi(\vec{r}, E, \vec{\Omega}) - \frac{\partial}{\partial E} (\beta_r(\vec{r}, E) \psi(\vec{r}, E, \vec{\Omega})) \\ + \nabla_v \cdot \left\{ \vec{a} \left(\frac{\psi(\vec{r}, E, \vec{\Omega})}{v} \right) \right\} - Q^{xy}(\vec{r}, E, \vec{\Omega}) = S(\vec{r}, E, \vec{\Omega}) \end{aligned} \quad (6.2)$$

where ∇_v is the del operator in velocity space, and \vec{a} is the acceleration. Equation (6.2) is the general relativistic LBTE for forces that create an acceleration \vec{a} . For the case where a magnetic force is present, Equation (6.2) can be expressed as (St. Aubin et al. 2015)

$$\begin{aligned} & \nabla_v \cdot \left\{ \vec{a} \left(\frac{\psi(\vec{r}, E, \vec{\Omega})}{v} \right) \right\} \\ &= \frac{q}{p} (\vec{\Omega} \times \vec{B})_z \frac{\partial \psi}{\partial \mu} + \frac{q}{p(1-\mu^2)} (\vec{\Omega} \times (\vec{\Omega} \times \vec{B}))_z \frac{\partial \psi}{\partial \phi} \end{aligned} \quad (6.3)$$

where p is the magnitude of the momentum, $\mu = \cos \theta$, and $(\bullet)_z$ denotes taking the z component of the cross product. Therefore, the final form of the magnetic force LBTE becomes

$$\begin{aligned} & \vec{\Omega} \cdot \nabla \psi(\vec{r}, E, \vec{\Omega}) + \sigma(\vec{r}, E) \psi(\vec{r}, E, \vec{\Omega}) - \frac{\partial}{\partial E} (\beta_r(\vec{r}, E) \psi(\vec{r}, E, \vec{\Omega})) \\ & - \frac{q}{p} (\vec{\Omega} \times \vec{B})_z \frac{\partial \psi(\vec{r}, E, \vec{\Omega})}{\partial \mu} - \frac{q}{p(1-\mu^2)} (\vec{\Omega} \times (\vec{\Omega} \times \vec{B}))_z \frac{\partial \psi(\vec{r}, E, \vec{\Omega})}{\partial \phi} \\ & - Q^{xy}(\vec{r}, E, \vec{\Omega}) = S(\vec{r}, E, \vec{\Omega}). \end{aligned} \quad (6.4)$$

Using a standard discrete ordinates (DO) approach, this mathematical formulation was shown to be extremely accurate, agreeing with Monte Carlo calculations (figures 6–37 and 6–38). The DO calculations were performed in an inhomogeneous slab phantom consisting of water, bone, and lung. The bone slab was placed directly anterior to the lung slab in order to test the new formalism in a challenging radiation transport scenario where the transport code must model the long path lengths in lung of the electrons ejected from the distal side of the bone. Quantitative analysis (Low et al. 1998) showed that greater than 99.8% of all points analyzed passed a 2%/2 mm gamma criterion for all field sizes investigated.

However, in the DO method, the angular partial derivatives seen in Equation (6.4) cannot be performed directly due to the nature of the angular discretization. The formalism, therefore,

relied on a spherical harmonic expansion of the angular fluence, allowing the angular derivatives to be calculated using the associated Legendre polynomial recursion relations (St. Aubin et al. 2015). The downside to this method was that for scenarios characterized with low-density materials and relatively strong magnetic fields, the iterative solution stagnated before meeting the required convergence tolerance. Although work is ongoing to understand this phenomenon within a DO framework, it was determined that an alternative angular discretization is required that would allow the angular derivatives to be calculated without a spherical harmonic expansion, therefore solving this problem.

With this hypothesis, a linear discontinuous finite element method (DFEM) discretization of the angular variables was developed (St. Aubin et al. 2016). Equation (6.4) can be recast as

$$\begin{aligned} & \vec{\Omega} \cdot \nabla \psi(\vec{r}, E, \vec{\Omega}) + \sigma(\vec{r}, E) \psi(\vec{r}, E, \vec{\Omega}) - \frac{\partial}{\partial E} (\beta_r(\vec{r}, E) \psi(\vec{r}, E, \vec{\Omega})) \\ & + \vec{\tau}(\vec{B}, E, \vec{\Omega}) \cdot \nabla_{\Omega} \psi(\vec{r}, E, \vec{\Omega}) - Q^{xy}(\vec{r}, E, \vec{\Omega}) = S(\vec{r}, E, \vec{\Omega}) \end{aligned} \quad (6.5a)$$

where

$$\vec{\tau}(\vec{B}, E, \vec{\Omega}) = \frac{q}{p\sqrt{1-\mu^2}} (\vec{\Omega} \times (\vec{\Omega} \times \vec{B}))_z \hat{\phi} - \frac{q}{p\sqrt{1-\mu^2}} (\vec{\Omega} \times \vec{B})_z \hat{\theta} \quad (6.5b)$$

and

$$\nabla_{\Omega} = \frac{1}{\sqrt{1-\mu^2}} \frac{\partial}{\partial \phi} \hat{\phi} + \frac{\partial}{\partial \theta} \hat{\theta} \quad (6.5c)$$

In this form, the magnetic force term resembles the spatial streaming operator—the first term in Equation (6.5a)—suggesting that the solution can be obtained through a space-angle sweep (St. Aubin et al. 2016). It was shown that by performing this space-angle sweep, stagnation of the iterative solution was eliminated. The novel linear DFEM space-angle calculations were again performed in an inhomogeneous slab phantom. The DFEM space-angle treatment of the magnetic force LBTE was first compared to Monte Carlo and the previous DO formalism

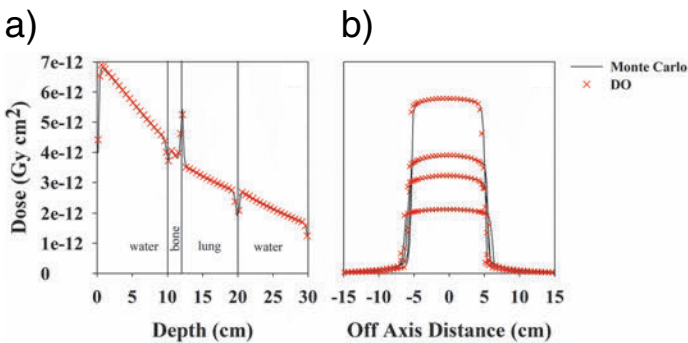


Figure 6–37. a) depth-dose along the central axis and b) y profiles at the center of the beam ($x = 0$) for a $10 \times 10 \text{ cm}^2$ field comparing Monte Carlo and the DO formalism in a 3 T magnetic field perpendicular to the radiation beam. From (St. Aubin et al. 2015).

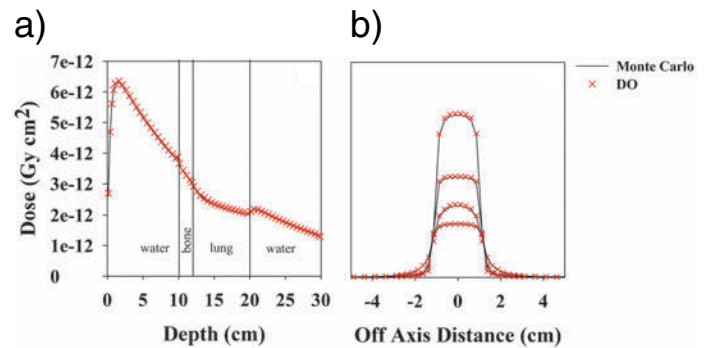


Figure 6–38. a) depth-dose along the central axis and b) y profiles at the center of the beam ($x = 0$) for a $2 \times 2 \text{ cm}^2$ field comparing Monte Carlo and the DO formalism in a 0.6 T magnetic field parallel to the radiation beam. From (St. Aubin et al. 2015).

in the same lung slab phantom as described above (Figure 6–39). The lung slab was then replaced by an air slab at standard temperature and pressure (mass density of $1.2 \times 10^{-3} \text{ g/cm}^3$) and validation of the DFEM space-angle formalism was performed

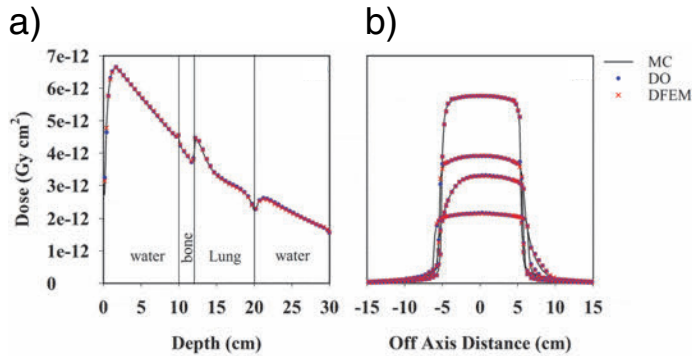


Figure 6–39. a) depth-dose along the central axis and b) x profiles at the center of the beam ($y = 0$) comparing Monte Carlo, discrete ordinates (DO) formalism, and the DFEM space-angle formalism in a 0.5 T magnetic field perpendicular to the radiation beam. From (St. Aubin et al. 2016).

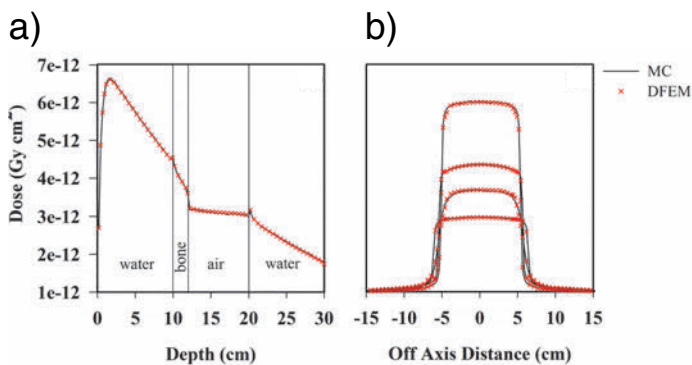


Figure 6–40. a) depth-dose along the central axis and b) x profiles at the center of the beam ($y = 0$) comparing Monte Carlo and the DFEM space-angle formalism in a 0.5 T magnetic field parallel to the radiation beam. From (St. Aubin et al. 2016).

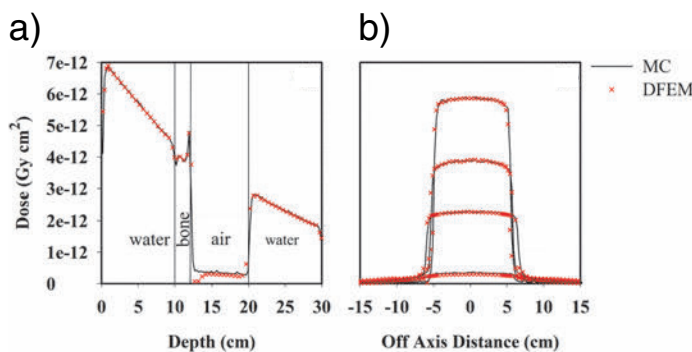


Figure 6–41. a) depth-dose along the central axis and b) x profiles at the center of the beam ($y = 0$) comparing Monte Carlo and the DFEM space-angle formalism in a 3 T magnetic field perpendicular to the radiation beam. From (St. Aubin et al. 2016).

against Monte Carlo. Despite the challenging nature of this problem due to the very long path lengths in air, the DFEM space-angle treatment was generally proven to be extremely accurate (figures 6–40 and 6–41). The dip in the DFEM solution immediately distal to the bone seen in Figure 6–41 is seen only for very steep dose gradients caused by large differences in material properties (bone to air) at very high magnetic fields. This behavior continues to be investigated, but is not seen at the Alberta linac-MR field strength of 0.5 T.

A highly accurate method of calculating radiotherapy doses in magnetic fields is a critical component of any linac-MR system. In light of this, a novel mathematical framework for including the magnetic force component of the Lorentz force was first presented by the Alberta linac-MR group (St. Aubin et al. 2015; St. Aubin et al. 2016) and has proven to be a highly accurate method of calculating radiotherapy doses in magnetic fields. Work continues on increasing the speed and efficiency of the deterministic calculations, but large speed-ups are expected with algorithm enhancements and by leveraging cluster-based or graphics processor unit (GPU) infrastructures.

6.3.4 Response of Radiation Detectors in Magnetic Field

The presence of a magnetic field alters the response of radiation detectors (Reynolds et al. 2013; Reynolds et al. 2014; Reynolds

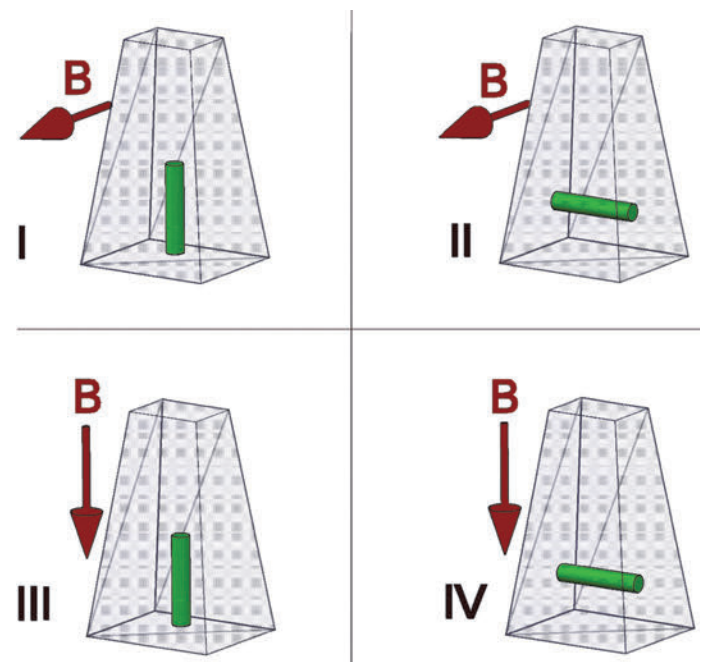


Figure 6–42. Various geometrical orientations for radiation detector's long axis (central cylinder) magnetic field (arrow) and radiation beam (transparent rectangular prism) as used in Monte Carlo simulation and experimental measurements. From (Reynolds et al. 2013).

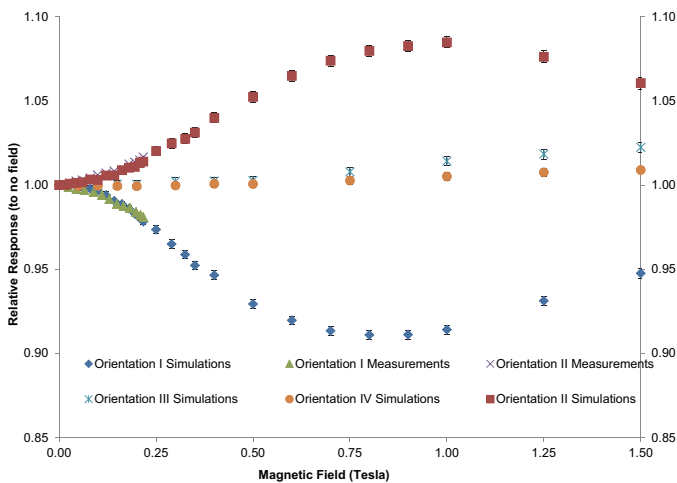


Figure 6–43. PRO6C relative dose deposited as a function of magnetic field strength in orientations I–IV for simulations, and orientations I and II for measurements. From (Reynolds et al. 2013).

et al. 2015; Meijsing et al. 2009), a phenomenon that needs to be characterized for accurate reference and relative dosimetry (Smit et al. 2012; Goddu et al. 2012). In our lab, we have investigated the dose response of various ionization chambers and solid state detectors within a magnetic field, either perpendicular (transverse: orientations I and II) or parallel (longitudinal: orientations III and IV) to the radiation beam travel. The detectors' long axis is either parallel (orientations I and III) or perpendicular (orientations II and IV) to the radiation beam travel (Figure 6–42). The well-benchmarked Monte Carlo code PENELOPE is used to model the dose deposition in the active volumes of the various detectors in air and in a water tank as a function of magnetic field strength in the orientations of interest. When physically possible, the dose response of the detectors in the relevant orientations is measured experimentally with the aid of small transverse and longitudinal electromagnets. The dose response of the detectors is defined as the ratio of dose for a detector reading with an applied magnetic field to that without a magnetic field.

Figure 6–43 shows the dose response of the PRO6 ion chamber. Initially, the dose response either decreases or increases with increasing transverse magnetic field when the long axis of the detector is either parallel or perpendicular to the radiation beam. As the magnetic field is increased further, the dose response changes toward unity. In longitudinal geometry, the response deviates minimally from unity. This response is representative of the other cylindrical ion chambers, suggesting that a chamber orientation and magnetic field-based correction factor is required for linac-MR systems with transverse magnetic field orientation to radiation beam travel. We have also simulated ion chamber response in TG-51-like conditions at a depth of 10 cm in water. The change in the response of an ion chamber under these conditions has a similar behavior, as shown

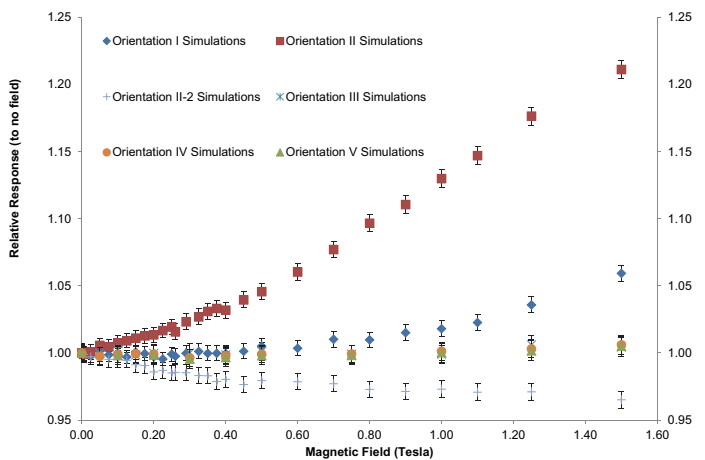


Figure 6–44. Monte Carlo generated dose response of the PTW60003 diamond detector as a function of magnetic field strength. Error bars are ± 1 standard deviation. From (Reynolds et al. 2014).

in Figure 6–42. Therefore, for MR-guided teletherapy systems, there will be an additional magnetic field-dependent correction factor for an ion chamber in a transverse magnetic field in addition to other standard factors, such as polarity and ion recombination, that do not change much due to the magnetic field (Smit et al. 2012; Goddu et al. 2012). Our results suggest that this additional correction factor is not needed if the radiation beam and magnetic field are in parallel (Reynolds et al. 2013; Reynolds et al. 2014; Reynolds et al. 2015).

The presence of a transverse magnetic field changes the beam penumbra in water, and we have found that cylindrical ion chambers have additional issues in measuring dose in the penumbra region in the presence of transverse magnetic fields. The altered chamber response does not correlate with the altered penumbra, requiring further investigation (Reynolds et al. 2014). Again, the correction factor for measuring penumbra in profiles is not needed in the parallel magnetic field case.

Although the effect of a magnetic field on an ion chamber's response is expected due to the curving of electrons within the chamber's air cavity, the magnetic field may also alter the response of solid state detectors. Figure 6–44 shows the relative response of a PTW diamond detector as a function of magnetic field strength. In the case where a magnetic field is transverse to the radiation field, the detector response rises monotonically as the magnetic field increases; the response increases faster when the detector long axis is perpendicular to the magnetic field. Similar to an anion chamber, the detector response minimally deviates from unity for a magnetic field oriented parallel to the radiation field. The diamond detector has a small air cavity in the structure housing the diamond, causing the change in the response. A similar response to a transverse magnetic field was also established for a typical photon diode detector, presumably

due to the presence of a tungsten shield, designed to reduce the directional anisotropy.

In conclusion, a careful study of the impact of a magnetic field on a radiation detector's response is required before reference or relative dosimetry is performed in an MR-guided teletherapy system. This is particularly true for linac-MR systems with a transverse magnetic field, but less so for the parallel magnetic field geometry.

6.4 Intra-fractional Tumor-tracked Irradiation

6.4.1 Overview of Intra-fractional Tumor Tracking

Both “intra-fractional tumor tracking” and “real-time tumor tracking” refer to the method of continuously tracking the tumor with the radiation beam during beam delivery. Intra-fractional tumor tracking is one of the most promising techniques aimed at minimizing normal tissue irradiation when treating mobile tumors. If this technique is accurately executed, the beam margin assigned for motion compensation may be significantly reduced or eliminated.

At present, however, a method of directly imaging tumors during beam delivery with sufficient soft tissue contrast does not exist. Thus, all currently available tracking systems rely on indirect tracking methods based on internal or external tumor surrogates (Vedam 2003; Nioutsikou 2008; Harada 2002).

A hybrid radiotherapy-MR system at the Cross Cancer Institute (CCI) overcomes the aforementioned limitation by enabling intrafractional MR imaging of a tumor, providing excellent soft tissue contrast. (Fallone 2009). Using the prototype linac-MR, we have investigated a direct, surrogate-free intra-fractional tumor tracking system. Our initial focus is given to lung tumor tracking, due to the potential for a lung tumor to

exhibit a large range of motion and shape deformation during treatment. A schematic representation of the tracking process is provided in Figure 6–45.

In step 1 of Figure 6–45, the linac-MR provides intra-fractional MR images of a lung tumor during normal breathing. The rate of MR imaging has been chosen to be approximately four frames per second (fps) in order to keep the system delay time under 500 ms, as recommended by the AAPM Task Group 76 report for lung tumor tracking (Keall 2006). Here, system delay refers to the time interval between the detection of the current tumor position (i.e., image acquisition) and the beam delivery upon the multileaf collimator (MLC) reaching its target position.

In step 2, tumor auto-contouring is applied to each MR image to determine the shape and position of the lung tumor. Currently, manual contouring of the tumor by an expert (e.g., a radiation oncologist) is considered the clinical “gold standard.” However, this would be too time consuming and negate the advantages of fast imaging in an actual clinical intrafractional tracking implementation. Thus, a rapid and reliable tumor auto-contouring algorithm is required, which will ideally lead to appropriate intrafractional radiation beam adjustment during treatment. Our group developed such an algorithm based on pulse-coupled neural networks (PCNN), and we demonstrated the feasibility of lung tumor auto-contouring in the linac-MR environment (0.5 T) via *in vivo* and phantom studies (Yun 2015). The algorithm successfully contoured the shape of a moving tumor from pseudo 0.5 T MR images. For four patients in an *in vivo* study (600 images per patient), the algorithm showed 87% to 92% contouring agreement with manual contours performed by an expert in terms of Dice's similarity index (DSI). An example image of the four patients is shown in Figure 6–46, and quantitative results are provided in Table 6–1.

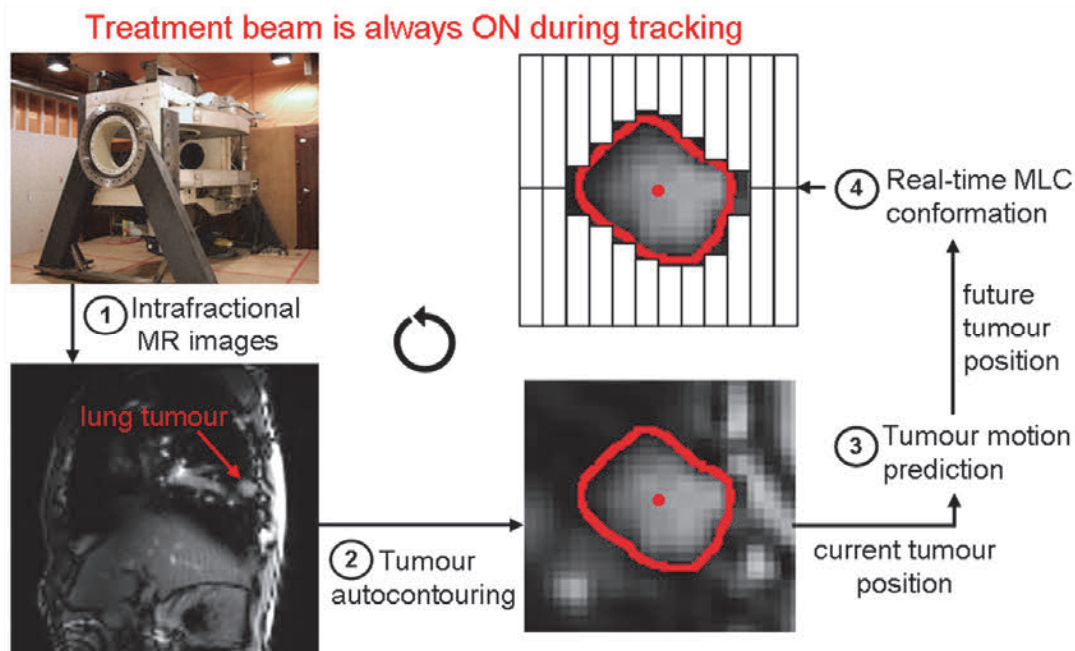


Figure 6–45. Overview of intrafractional tumor tracking process. Steps 1–4 are repeated for every intra-fractional MR image during tracking when the treatment beam is always on.

Table 6–1: Summary of contour shape fidelity and centroid position accuracy ($\Delta d_{\text{centroid}}$: difference in centroid positions between manual and auto-contour). 600 images were compared for each patient.

Patient	DSI		Hausdorff Distance (mm)		$\Delta d_{\text{centroid}}$ (mm)	
	Mean (SD)	Max/Min	Mean (SD)	Max/Min	Mean (SD)	Max/Min
1	0.90 (0.03)	0.97 / 0.76	3.38 (0.95)	6.43 / 1.56	1.04 (0.53)	3.77 / 0.05
2	0.89 (0.03)	0.95 / 0.76	4.35 (1.26)	9.49 / 1.56	1.35 (0.71)	4.08 / 0.02
3	0.87 (0.05)	0.98 / 0.66	3.13 (1.41)	7.95 / 1.56	1.03 (0.63)	3.79 / 0.01
4	0.92 (0.03)	0.98 / 0.83	4.11 (1.49)	11.03 / 1.56	1.31 (0.70)	4.00 / 0.06

In step 3 of Figure 6–45, tumor motion prediction occurs based on the current tumor position (i.e., position of tumor centroid) detected by tumor auto-contouring. Ideally, intrafractional tracking would provide tumor detection and beam delivery simultaneously. However, there exists an inevitable system delay between the two events due to (1) the time requirement to drive each leaf of the MLC to its designated position, (2) image acquisition, and (3) computing/processing time. To compensate for this system delay, we developed a tumor motion prediction algorithm based on artificial neural networks (ANN) and evaluated its performance using tumor motion data from 29 lung cancer patients (Yun 2012). The prediction algorithm is designed to be flexible, accommodating various ranges of system delays and frequencies of tumor position detection. From the most relevant scenario in our linac-MR environment (~4 fps imaging rate,

~300 ms system delay), the prediction accuracy was shown to be 0.7–0.8 mm in terms of mean RMSE between the true and predicted tumor positions in each patient data.

The predicted future tumor position is input to step 4 of Figure 6–45 for real-time MLC conformation, which is conducted by an MLC controlling system built in-house. Steps 1–4 are repeated for every intrafractional MR image during tracking while the treatment beam is always on.

6.4.2 Proof of Concept: Linac-MR Tumor-tracked Irradiation

The world's first proof of concept demonstration of MR image-controlled intrafractional lung tumor-tracked irradiation was performed using the first prototype linac-MR system at the CCI in 2012 (Yun 2013). The in-house tracking system operates

	(a) Pseudo-0.5T MR images	(b) Expert contour	(c) Software contour	(d) Comparison (white: overlap red: difference)	DSI (%)
Patient 1					97 %
Patient 2					95 %
Patient 3					97 %
Patient 4					98 %

Figure 6–46. Example images of the four patients. Column (a) example lung tumor images (pseudo-0.5 T). Columns (b) and (c) Expert's manual contour and software-generated autocontour. (d) comparison between manual and auto-contour (overlapping region is shown in white pixels, whereas any deviation is indicated by red pixels). Taken from (Yun et al. 2015).

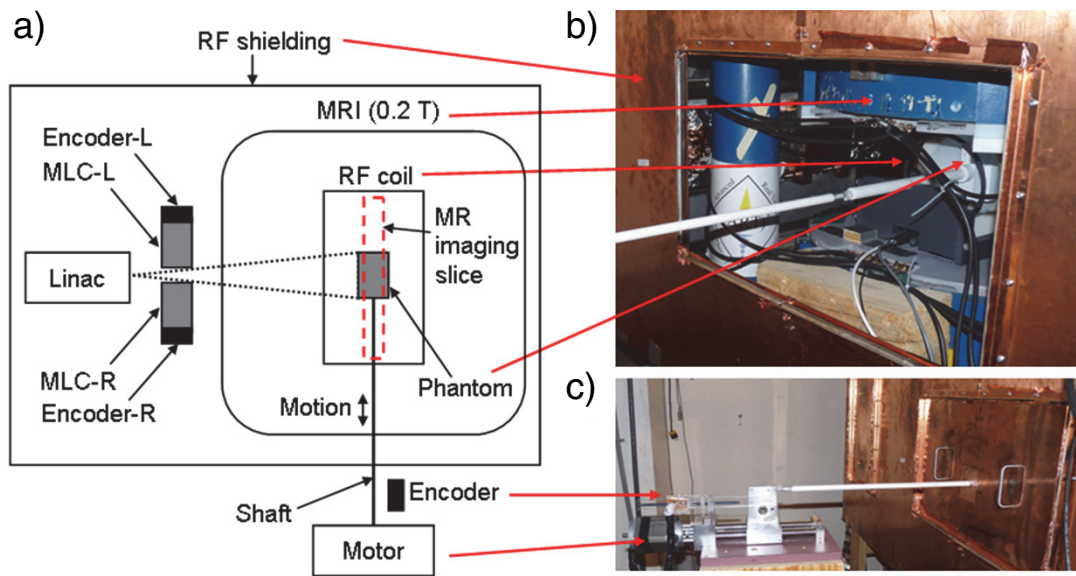


Figure 6–47. Linac-MR and motion phantom setup: a) basic diagram of entire setup (top-down view), b) linac-MR and phantom setting with RF cage open, c) side view with RF cage closed. Taken from (Yun et al. 2013).

intrafractional MR imaging, tumor auto-contouring, motion prediction, and MLC control while the treatment beam is always on, as described in Figure 6–45. The linac-MR system used for demonstration is equipped with a 6 MV linac and 0.2 T MRI, as shown in Figure 6–47 (beam direction is perpendicular to the main magnetic field), providing dynamic MR imaging at 4 fps.

During tracking, an MR-compatible motion phantom was used to reproduce tumor motions, as shown in Figure 6–47. The phantom is made of two symmetrical parts, as shown in Figure 6–48a. The central custom-shaped target representing a tumor volume is made of porcine skin gelatin. An MR image of this phantom acquired during the tracking experiment is shown in Figure 6–48c. The phantom was driven to create 1D motion along the axis of the RF coil, as indicated in Figure 6–48d, which creates phantom motion in the direction perpendicular to

the x-ray beam along the leaf motion direction of the MLC. Gafchromic film was inserted between the two cases to measure radiation exposure during tracking.

We demonstrated intrafractional MR tumor tracking using two different motion patterns: (1) a sine pattern (period: 6.7 s, motion range: 4 cm, max. speed: 1.8 cm/s) representing ideal, periodic tumor motions, and (2) a modified cosine pattern (period: 5.1 s, motion range: 4 cm, max. speed: 3.1 cm/s) representing more realistic lung tumor motions. For each motion pattern, four different treatment scenarios were tested with a 2 min beam on time (100 MU/min) as summarized in Table 6–2. Scenario 1 (S1) simulates the situation of applying the maximum beam margin around the target covering the full extent of target motion, whereas S4 simulates the most advanced tracking scenario, including motion prediction without beam margin.

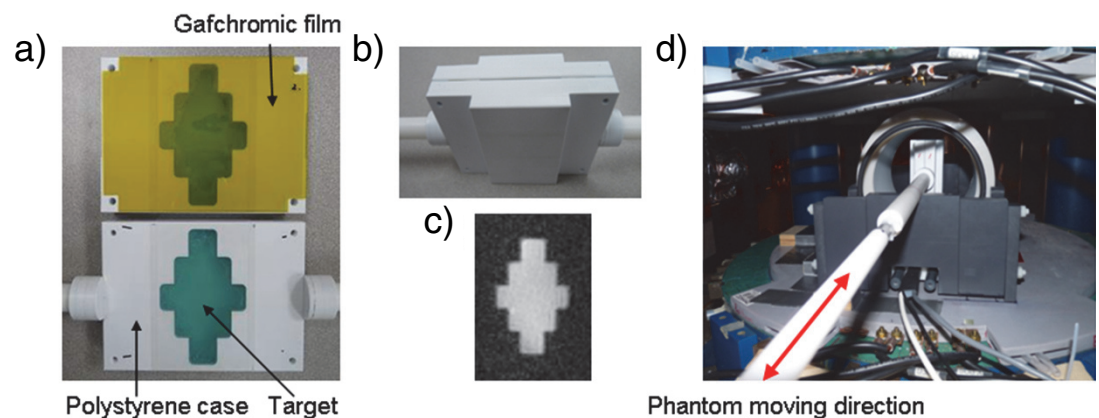


Figure 6–48. Motion phantom: a) phantom parts, b) assembled phantom, c) MR image during tracking and beam delivery, d) phantom and RF coil placed in the linac-MR. Taken from (Yun et al. 2013).

Table 6–2: Treatment scenarios tested

	Scenario 0 (S0)	S1	S2	S3	S4
Phantom motion	No	No	Yes	Yes	Yes
Beam margin	None	Maximum	None	None	None
MLC tracking	No	No	No	Yes	Yes
Motion prediction	No	No	No	No	Yes

Table 6–3: Beam and penumbra width in different scenarios

Phantom motion	None		Sine			Modified Cosine		
Tracking scenario	S0	S1	S2	S3	S4	S2	S3	S4
50% beam width (mm)	62.5	103.4	63.5	62.4	62.0	63.6	61.9	62.2
80–20 % penumbra width (mm)	6.9	7.0	33.0	11.5	7.3	34.1	15.8	8.6

Figure 6–49 shows the positional changes of the phantom and each MLC leaf during tracking through encoder readings. By comparing S3 and S4, it is clearly shown that the different amount of system delays in the two motion patterns is compensated by implementing motion prediction capability in our tracking system.

Figure 6–50 shows the films exposed in different tracking scenarios (S0–S4). The open-beam dose profiles are not flat due to a slight misalignment of the beam and the flattening filter in the linac-MR. From visual inspection, the shape of the high-dose region covering the target in S4 films show the sharpest edges compared to the blurred ones shown in S2 and S3 films. Potential beam margin reduction using our tracking system is clearly observed comparing S1 to S4 films. Quantitative analysis is provided in Table 6–3 in terms of (1) beam width at 50%, and (2) 80% to 20% penumbra width from the dose profile in each tracking scenario.

As shown in Table 6–3, we were able to deliver highly conformal dose to a moving target using predictive tumor tracking. Compared to static target irradiation, the 50% beam width remains virtually unchanged (<0.5 mm), and the increase in 80% to 20% penumbra width is less than 1.7 mm during the

irradiation of a moving target. These results illustrate the potential dosimetric advantages of intrafractional MR tumor tracking in treating mobile tumors by significantly reducing or eliminating the beam margin assigned for motion compensation.

6.5 MR Imaging for Radiotherapy

6.5.1 Geometric Image Distortion: Overview

The use of MR images for treatment planning or real-time tumor tracking during radiotherapy involves some severe geometric constraints not normally relevant to imaging for diagnostic purposes. While the geometric deformation of an image of several mm or more will not generally compromise the diagnostic utility of an MR image, the consequence of treating a patient based on an image with severely misplaced tissue structures could be catastrophic. To this end, any linac-MR hybrid system must give serious consideration to all sources of potential distortion and make sure each is properly addressed in a robust and reliable manner. It is typical for most modern commercial MR imaging systems to include integrated distortion-correction software, in part because of the compromises manufacturers have had to make to generate magnets with large, open bores and strong gra-

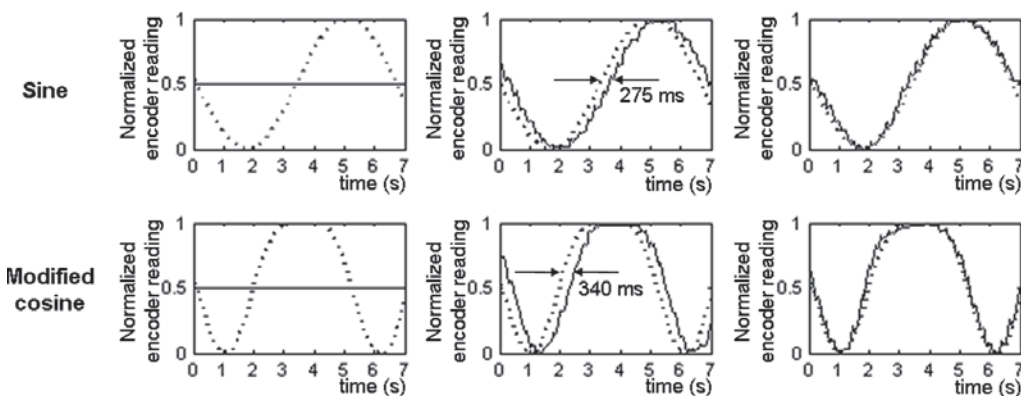


Figure 6–49. Encoder reading comparisons from phantom and MLC (recorded every 50 ms during tracking). The readings correspond to scenarios S2–S4, and the two motion patterns are shown. Taken from (Yun et al. 2013).

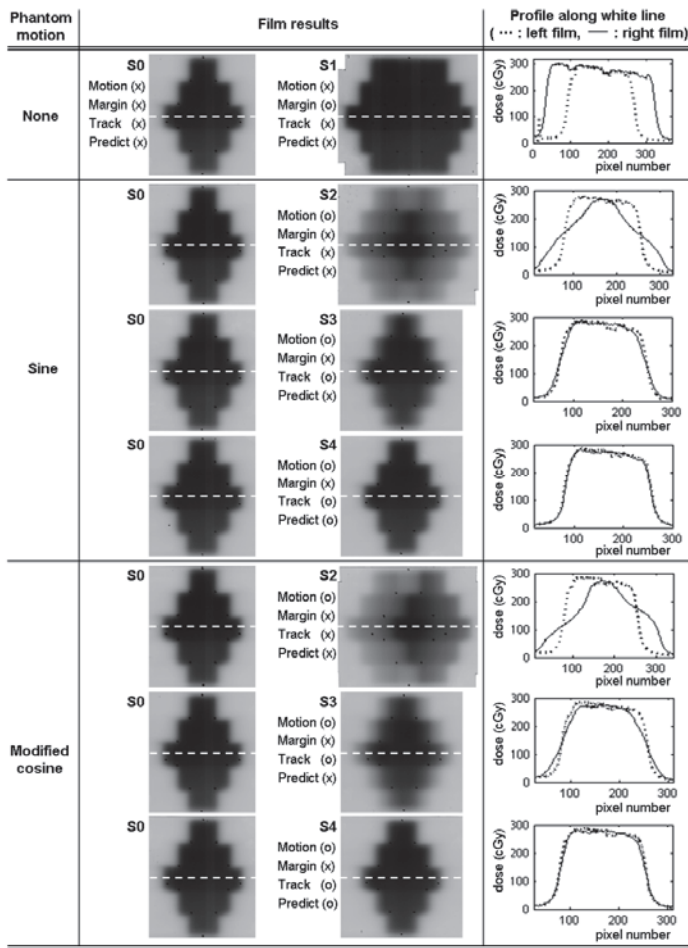


Figure 6–50. Film measurements in different scenarios using the sine and modified cosine motion patterns. Taken from (Yun et al. 2013).

dient fields with rapid slew rates (Janke et al. 2004). However, given that the performance of these integrated software packages are largely driven by the geometric demands of diagnostic imaging, one must consider that they may not perform to a degree of accuracy appropriate for radiotherapy. Indeed, assessments of vendor-supplied corrections of geometric distortion have revealed levels of residual distortions that would pose a problem for radiotherapy guidance (Wang et al. 2004). As such, a physicist should be hesitant to rely solely on the vendor-supplied correction software for radiotherapy purposes unless (1) the technique used by the vendor is well understood, and (2) extensive quantitative testing with a phantom reveals the software to provide results that satisfy the stringent requirements of the clinical program in question. Furthermore, the vendor-supplied correction will only account for major system-related distortion sources, namely gradient-field nonlinearity, and background magnetic field (B_0) inhomogeneity. Other important sources, such as patient-dependent field inhomogeneities due to the unique arrangement of tissues with differing constants of magnetic susceptibility, can generate sizable geometric distortions

depending on the B_0 field strength and the MRI pulse sequence used. These distortions will likely have to be controlled or corrected through a specially designed module.

6.5.2 General Correction Methodology

In order to correct for geometric distortion, one must be able to measure or calculate the distortion field (the distortion field being a matrix of vectors describing the shift of each image voxel from its true source location). With a phantom containing an array of geometric features with a known spatial distribution, this distortion field could technically be measured for every sequence of interest. (Any B_0 inhomogeneity, whether system- or patient-related, will contribute to the distortion field in a manner that is dependent on MR pulse-sequence type and implementation.) However, this approach would be extremely time consuming, as key imaging parameters invariably differ from patient to patient. Instead, if one can characterize both the nonlinearity of the gradient fields as well as the B_0 inhomogeneity, it can be shown that the distortion fields can be predicted for all subsequently acquired images (so long as the two field characterizations remain valid) (Baldwin et al. 2009). Thus, the success of any distortion correction procedure in MRI is strongly dependent on the quality of gradient and B_0 field characterization. Examples of geometric distortion correction over multiple scans utilizing these B_0 /gradient characterizations are shown in figures 6–51 and 6–52 for a phantom and male pelvis, respectively.

Characterization of gradient field nonlinearity

Spatial localization in MRI relies on the use of gradient coils that produce temporary magnetic fields within the magnet bore that, in an ideal world, vary linearly in space. There are three such coils that produce linear field variations in each of the three cardinal axes. Standard image reconstruction relies on the naive assumption of perfect linearity, an assumption that results in geometric distortion when invalid. Gradient nonlinearity contributes to the distortion field in a consistent way; regardless of the MR pulse sequence used, the effect of the nonlinear gradient fields on geometric distortion remains the same. Therefore, provided that there are no physical changes to the gradient set within the MRI unit, a single characterization of these fields can be used to define the gradient-related component of the distortion field for all subsequent scans. Of course, it is prudent to repeat these characterizations on a somewhat regular basis should some unknown incident have affected the physical positioning of the gradient coils.

To characterize the nonlinear nature of a gradient field, it is necessary to employ a phantom with a known geometric arrangement of features or control points. A number of phantom concepts have been investigated, including grid structures (Wang et al. 2004; Baldwin et al. 2009), and arrangements of fluid-filled rods (Doran et al. 2005) or spheres (Jovicich et al. 2006). Each concept may have its advantages, but all will suffice, provided the true position of each feature is known a priori.

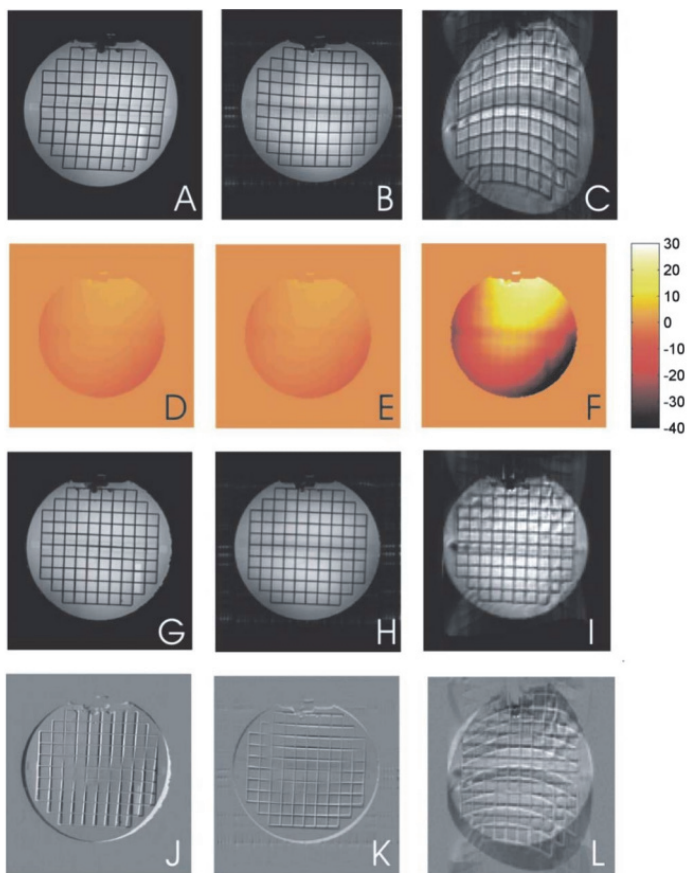


Figure 6–51. Validation of multi-image distortion correction using a grid phantom and a single-field distortion map. (a)–(c) Gradient echo, spin echo, and echo planar images of the grid phantom. Note: An unrelated zipper artifact and ghosting are seen in source images (b) and (c), respectively. (d)–(f) Sequence-dependent (resulting from B_0 distortion) spatial distortion maps for images (a)–(c), shown in millimeters. (g)–(i) Images shown in (a)–(c) corrected for both sequence-dependent and sequence-independent (gradient) spatial distortions. (j)–(l) Difference maps for images (a)/(g), (b)/(h), and (c)/(i). From (Baldwin et al. 2009).

If it was not for the complicating influence of the B_0 field inhomogeneity, the distortion field resulting from the gradients could simply be discerned by comparing the positions of control points on an acquired image to their known true positions. However, any B_0 inhomogeneity present during this characterization scan will cause a spatial shift along the orientation of the read-encoding gradient. To filter out this contribution, a “reverse-gradient” technique can be used where two scans are carried out that are identical in every way except for the polarity of their read-encoding gradient (Chang et al. 1992; Baldwin et al. 2007). As a result, the spatial shift resulting from the B_0 inhomogeneity will be completely opposite between the two scans. A simple average of control-point location will then reveal the position of the control point as distorted by the gradient fields alone.

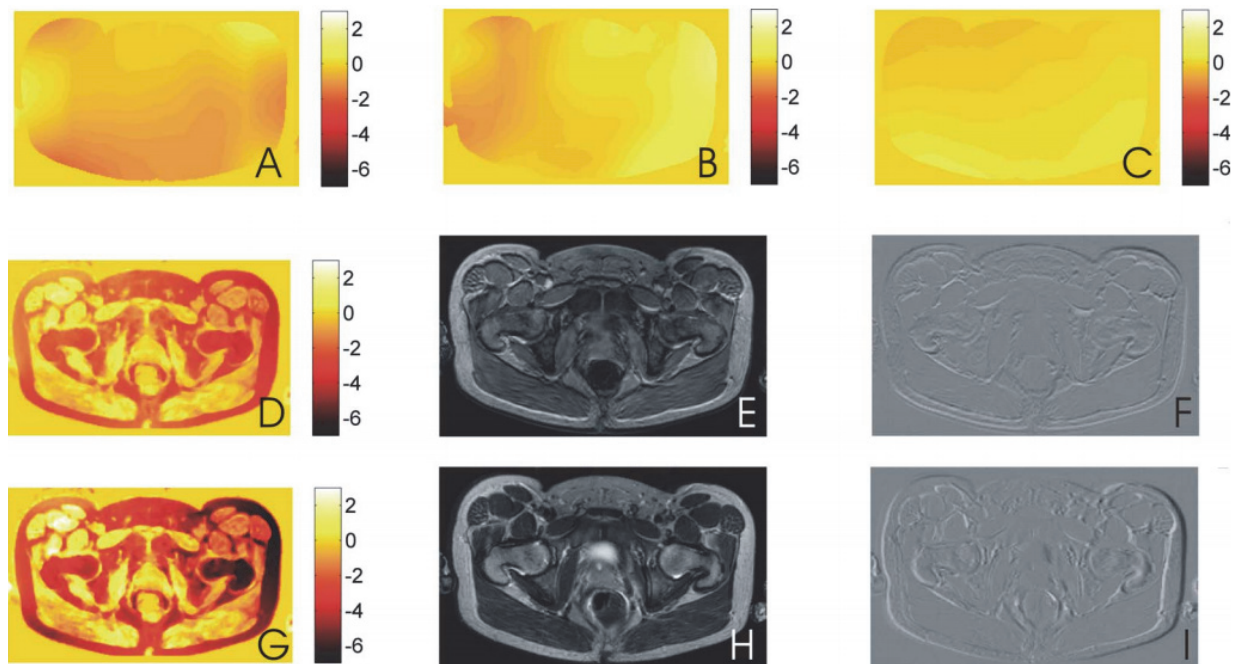


Figure 6–52. Distortion correction for gradient-echo (GE) images (d to f) and spin-echo (SE) images (g–i) of a male volunteer. (a) x-gradient nonlinearity distortions (mm). (b) y-gradient nonlinearity distortions (mm). (c) z-gradient nonlinearity distortions (mm). (d) sequence-dependent spatial distortions (mm) for the GE sequence. (e) Original GE image. (f) Difference map corrected original. (g) Sequence-dependent distortions (mm) for the SE sequence. (h) Original SE image. (i) Difference map corrected original. From (Baldwin et al. 2009).

Characterization of an inhomogeneous B_0 field

The method used to determine the distribution of B_0 inhomogeneity will depend on whether the effects of heterogeneous tissue magnetic susceptibility are taken into account. If it is judged that this tissue contribution is small enough to be neglected, only the native B_0 inhomogeneity originating from the MR system itself need be characterized. (See the next section for a discussion regarding the factors that need to be considered for this decision.) The system inhomogeneity can be measured in a number of ways. For example, a single field probe (NMR magnetometer) can be rastered over a 3D volume to generate a matrix of values throughout the bore, or a collection of field probes arranged along a half-circle (known as a field camera) can be rotated through 360 degrees to generate magnetic field values over the surface of a sphere. These methods are typically used when performing on-site shimming of the magnet during installation or hardware upgrades. However, this B_0 distribution can also be determined from the data already acquired during the characterization of gradient nonlinearity described above. A simple subtraction of the mean image control point locations (containing only distortions from gradient nonlinearity) from

those derived from one of the two source image sets (containing distortions from both gradient nonlinearity and B_0 inhomogeneity) will yield a spatial shift originating from the variations in B_0 alone (Baldwin et al. 2007).

It is important to note that a number of factors—including the use of active shim circuits during subsequent scans and the change of magnet position relative to objects or equipment in the vault—will serve to alter this baseline B_0 characterization and must be taken into account. The magnetic fields associated with the active shim circuits can, in general, be described analytically, and thus it is relatively straightforward to adjust the B_0 characterization accordingly. The impact of relative motion between the MR unit and objects in the vault (or the vault itself in the case of rotating units) is more complicated, and it will require careful measurements to determine the magnitude of these field fluctuations and characterize them to correct, if necessary (Wachowicz et al. 2012).

The characterization of B_0 variation that includes the effects of tissue magnetic susceptibility must be derived in a different way from the examples given above. Since a field probe or phantom containing control points are clearly impossible to use

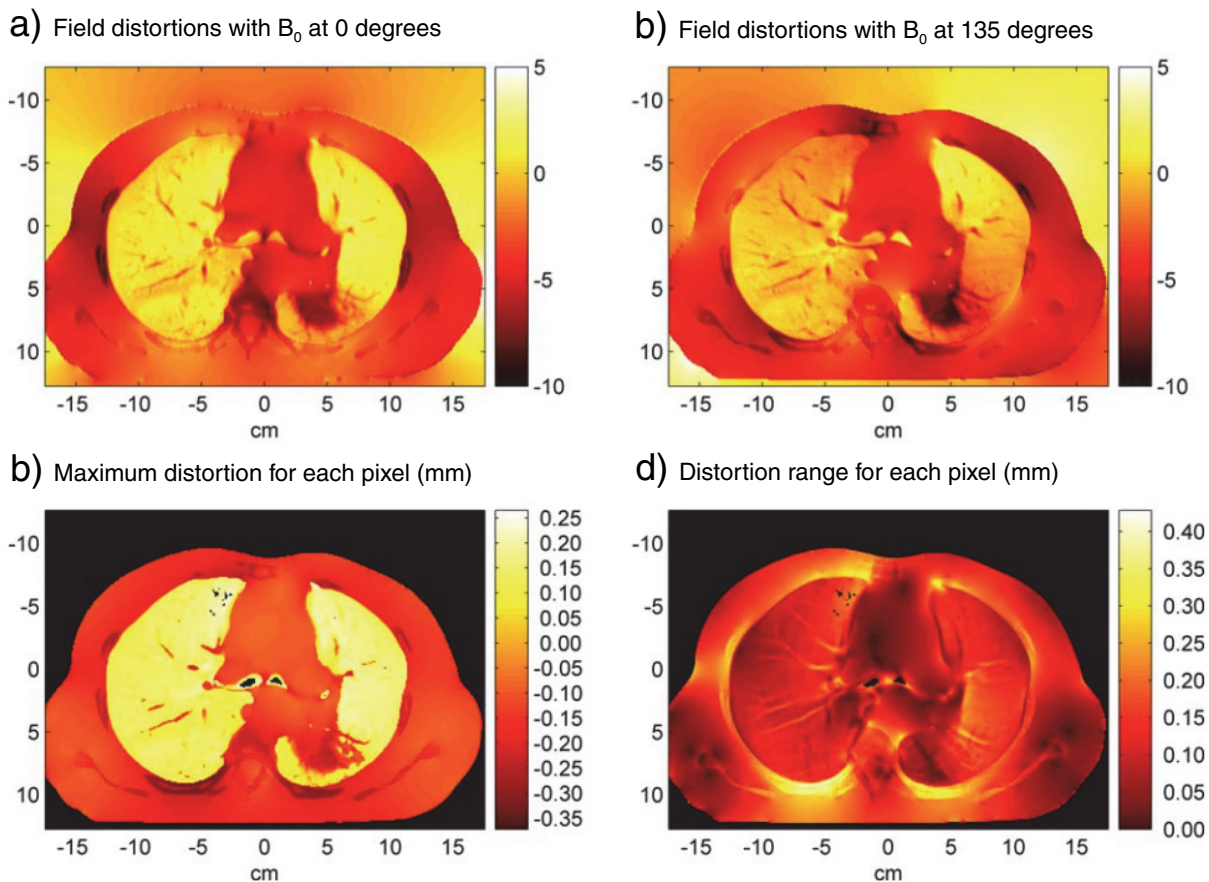


Figure 6–53. a) and b) Examples of the magnetic field maps for the lung site and how they were found to vary with magnetic field angle (ppm); a) was simulated with B_0 oriented at 0° degrees and b) at 135° . c) Illustrates the maximum distortion found for each soft-tissue pixel throughout a complete magnet revolution. d) Illustrates the range of field experienced by each soft-tissue pixel through a magnet revolution. From (Wachowicz et al. 2010).

Table 6–4: Maximum field distortions experienced by a voxel within the specified anatomic zone over a complete revolution of the magnet. Distortions that are greatest in magnitude are given, as well as the greatest range of field fluctuation as the magnet rotates. The corresponding geometric distortions for three field strengths are also given, assuming an encoding gradient strength of 5 mT/m. All these results are quoted first for the case where only a single frequency correction is performed, and then for the case where a frequency correction is performed at each magnetic rotation angle.

From (Wachowicz et al. 2010).

	Anatomical zone	Max distortion (ppm)	Max distortion range (ppm)	Consequence in mm at 0.2 T (5 mT/m)		Consequence in mm at 0.5 T (5 mT/m)		Consequence in mm at 1.5 T (5 mT/m)	
				Max distortion	Max range	Max distortion	Max range	Max distortion	Max range
Single f_0 correction	Brain	7.12	11.27	0.3	0.5	0.7	1.1	2.1	3.4
	Prostate	–8.17	9.82	–0.3	0.4	–0.8	1.0	–2.5	2.9
	Prostate/air	–8.18	10.56	–0.3	0.4	–0.8	1.1	–2.5	3.2
	Lung	–8.64	13.46	–0.3	0.5	–0.9	1.3	–2.6	4.0
Multiple f_0 corrections	Brain	7.11	11.49	0.3	0.5	0.7	1.1	2.1	3.4
	Prostate	–8.17	10.34	–0.3	0.4	–0.8	1.0	–2.5	3.1
	Prostate/air	–8.18	10.34	–0.3	0.4	–0.8	1.0	–2.5	3.1
	Lung	–7.64	13.62	–0.3	0.5	–0.8	1.4	–2.3	4.1

with a patient on the table, the field data must be derived from NMR measurements on the tissue itself. To this end, a so-called multi-gradient-echo sequence can be performed in which two images are obtained simultaneously using two data readouts separated by a constant time delay, or echo-spacing. Since the measured NMR resonance frequency is known to be linearly proportional to the magnetic field experienced by the nuclei according to the Larmor equation (Haacke et al. 1999), the phase difference measured between the images acquired at the two different echo times can be used to determine the patient-specific B_0 distribution (Baldwin et al. 2009).

Distortion from tissue magnetic susceptibility: when to correct

The decision of whether or not to include the effects of heterogeneous tissue magnetic susceptibility in a correction scheme depends on a number of factors, including the field strength of the MR unit in question, as well as the read-encode gradient strength (or effective gradient strength in the case of echo-planar imaging). Although the procedure for determining this tissue-based distribution is relatively straightforward (described in the section above), in practice it is not always a trivial matter to solve for these field maps. This difficulty originates from the necessity to unwrap the phase difference map, which can sometimes traverse multiple spans of 2π . This unwrapping can be practically difficult in image regions with low SNR or the presence of artifacts (from breathing, for example). Because of this occasional difficulty—compounded by the need to acquire the B_0 map at the onset of each patient session, which would serve to add time to each treatment session—it is logical to avoid this correction where possible. Previous studies have investigated the magnitude of spatial shifts that can be expected from tissue susceptibility (Wachowicz et al. 2010). An example of these susceptibility fields and resulting spatial shifts (assuming a read gradient of 5 mT/m) are displayed in Figure 6–53 for lung with

the B_0 field oriented transversely over a full range of possible angles. Numerical values are summarized in Table 6–4 for a number of different anatomies. Given the same sequence parameters, the spatial shifts resulting from the same tissue distribution will scale inversely with gradient strength and linearly with field strength. Therefore, there will be more flexibility for ignoring the effects of susceptibility at lower B_0 fields. For example, at a field of 0.5 T, the maximum distortions were found to be generally less than 1 mm using a 5 mT/m read gradient. However, if one sacrifices some flexibility and limits scanning to higher read gradient strengths, the same small shifts could be achieved at a larger B_0 field.

6.6 Conclusion

As discussed above, the interferences between the MRI and the linac have been resolved. It is now up to the oncology community to implement the linac-MR hybrids into the clinic and develop clinical protocols to best utilize and evaluate the technology to achieve the best clinical outcomes possible for all tumors currently treated by radiation and others—such as in the abdominal regions, liver, kidney, pancreas, etc.—not typically treated by radiation.

6.7 References

- Abdel-Rahman, W., J.P. Seuntjens, F. Verhaegen, and E.B. Podgorsak. (2006). “Radiation induced currents in parallel plate ionization chambers: measurement and Monte Carlo simulation for megavoltage photon and electron beams.” *Med. Phys.* 33:3094–3104.
- Baillie, D., J. St. Aubin, B.G. Fallone, and S. Steciw. (2015). “FEM design and simulation of a short, 10 MV, S-band linac with Monte Carlo dose simulations.” *Med. Phys.* 42:2044–53.
- Baldwin, L., K. Wachowicz, S. Thomas, R. Rivest, and B.G. Fallone. (2007). “Characterization, predication, and correction of geometric distortion in 3T MR images.” *Med. Phys.* 34:388–99.

- Baldwin, L.N., K. Wachowicz, B.G. Fallone. (2009). "A two-step scheme for distortion rectification of magnetic resonance images." *Med. Phys.* 36:3917–26.
- Bielajew, A.F. (1993). "The effect of strong longitudinal magnetic fields on dose deposition from electron and photon beams." *Med. Phys.* 20:1171–79.
- Burke, B., M. Lamey, S. Rathee, B. Murray and B.G. Fallone. (2009). "Radio frequency noise from clinical linear accelerators." *Phys. Med. Biol.* 54:2483–92.
- Burke, B., A. Ghila, B.G. Fallone, and S. Rathee. (2012a). "Radiation induced current in the RF coils of integrated linac-MR systems: the effect of buildup and magnetic field." *Med. Phys.* 39:5004–14.
- Burke, B., B.G. Fallone, and S. Rathee. (2010). "Radiation induced currents in MRI RF coils: application to linac/MRI integration." *Phys. Med. Biol.* 55:735–46.
- Burke, B., K. Wachowicz, B.G. Fallone, and S. Rathee. (2012b). "Effect of radiation induced on the quality of MR images in an integrated linac-MR system." *Med. Phys.* 39:6139–47.
- Case, R.B., J. Sonke, D.J. Moseley, J. Kim, K.K. Brock, and L.A. Dawson. (2009). "Inter- and intrafraction variability in liver position in non-breath-hold stereotactic body radiotherapy." *Int. J. Radiat. Oncol. Biol. Phys.* 75:302–08.
- Chang, H., and J.M. Fitzpatrick. (1992). "A technique for accurate magnetic resonance imaging in the presence of field inhomogeneities." *IEEE Trans. Med. Imaging* 11:319–29.
- Chen, Y., A.F. Bielajew, D.W. Litzenberg, J.M. Moran, and F.D. Becchetti. (2005). "Magnetic confinement of electron and photon radiotherapy dose: a Monte Carlo simulation with a non-uniform longitudinal magnetic field." *Med. Phys.* 32:3810–18.
- Constantin, D.E., L. Holloway, P.J. Keall, and R. Fahrig. (2014). "A novel electron gun for inline MRI-linac configurations." *Med. Phys.* 41:022301.
- Crijns, S., and B. Raaymakers. (2014). "From static to dynamic 1.5T MRI-linac prototype: impact of gantry position related magnetic field variation on image fidelity." *Phys. Med. Biol.* 59:3241–47.
- Degenhart, H.J., and W. Schlosser. (1961). "Transient effects of pulsed nuclear radiation on electronic parts and materials." *IRE Transactions on Component Parts* 124–28.
- Dempsey, J.F., D. Benoit, J.R. Fitzsimmons, A. Haghghat, J.G. Li, D.A. Low, S. Mutic, J.R. Palta, H.E. Romeijn, and G.E. Sjoden. (2005). "A device for real-time 3D image-guided IMRT." *Int. J. Radiat. Biol.* 63:1095.
- Doran, S.J., L. Charles-Edwards, S.A. Reinsberg, and M.O. Leach. (2005). "A complete distortion correction for MR images: I. Gradient warp correction." *Phys. Med. Biol.* 50:1343–61.
- Fallone, B.G. (2003). "Equipment for 'the move to image-guided and adaptive radiation therapy'." *Med. Phys.* 30:1937.
- Fallone, B.G., B. Murray, S. Rathee, T. Stanescu, S. Steciw, S. Vidakovic, E. Blosser, D. Tymofichuk. (2009). "First MR images obtained during megavoltage photon irradiation from a prototype integrated linac-MR system." *Med. Phys.* 36:2084–88.
- Fallone, B.G. (2007). "Equipment for move to image-guided and adaptive radiation therapy." *Med. Phys.* 30:1937.
- Fallone, B.G. (2014). "The rotating biplanar linac-magnetic resonance imaging system." *Semin. Radiat. Oncol.* 24:200–02.
- Fallone, B.G., M. Carlone, B. Murray, S. Rathee, T. Stanescu, S. Steciw, K. Wachowicz, C. Kirkby. (2007). "Development of a linac-MRI system for real-time ART." *Med. Phys.* 34:2547.
- Goddu, S., O. Pechenaya Green, and S. Mutic. "TG-51 calibration of first commercial MRI-guided IMRT system in the presence of 0.35 tesla magnetic field." (2012). *Med. Phys.* 39:3968 (abstract).
- Haacke, E.M, R.W. Brown, M.R. Thompson, and R. Venkatesan. *Magnetic Resonance Imaging: Physical Principles and Sequence Design*. New York: John Wiley & Sons, 1999.
- Halbach, H., and R.F. Holsinger. (1976). "Superfish – a computer program for evaluation of RF cavities with cylindrical symmetry." *Part. Accel.* 7:213–22.
- Harada, T., H. Shirato, S. Ogura, S. Oizumi, K. Yamazaki, S. Shimizu, R. Onimaru, K. Miyasaka, M. Nishimura, and H. Dosaka-Akita. (2002). "Real-time tumor-tracking radiation therapy for lung carcinoma by the aid of insertion of a gold marker using bronchofiberscopy." *Cancer* 95:1720–27.
- Janke, A., H. Zhao, G.J. Cowin, G.J. Galloway, D.M. Doddrell. (2004). "Use of spherical harmonic deconvolution methods to compensate for nonlinear gradient effects on MRI images." *Magn. Reson. Med.* 52:115–22.
- Jin, J. *The Finite Element Method in Electromagnetics*. New York: John Wiley & Sons, Inc., 2002.
- Johns, H.E., N. Aspin, and R.G. Baker. (1958). "Currents induced in the dielectrics of ionization chambers through the action of high energy radiation." *Radiat. Res.* 9:573–88.
- Jovicich, J., S. Czanner, D. Greve, E. Haley, A. van der Kouwe, R. Gollub, D. Kennedy, F. Schmitt, G. Brown, J. MacFall. (2006). "Reliability in multi-site structural MRI studies: effects of gradient non-linearity correction on phantom and human data." *Neuroimage* 30:436–43.
- Karzmark, C.J. *Medical Electron Accelerators*. New York: McGraw-Hill, Inc., 1993.
- Kawrakow, I., E. Mainegra-Hing, D.W.O. Rogers, F. Tessier, and B.R. Walters. (2009). "The EGSnrc code system: Monte Carlo simulation of electron and photon transport." Ottawa: National Research Council of Canada.
- Keall, P. J., G.S. Mageras, J.M. Balter, R.S. Emery, K.M. Forster, S.B. Jiang, J.M. Kapatoes, D.A. Low, M.J. Murphy, B.R. Murray, C.R. Ramsey, M.B. Van Herk, S.S. Vedam, J.W. Wong, and E. Yorke. (2006). "The management of respiratory motion in radiation oncology. Report of AAPM Task Group 76." *Med. Phys.* 33:3874–3900.
- Keyvanloo, A., B. Burke, B. Warkentin, T. Tadic, S. Rathee, C. Kirkby, D.M. Santos, and B.G. Fallone. (2012). "Skin dose in longitudinal and transverse linac-MR using Monte Carlo and realistic 3D MRI field models." *Med. Phys.* 39:6509–21.
- Khan, F. *The Physics of Radiation Therapy*. New York: Lippincott Williams & Wilkins, 2003.
- Kirkby, C., B. Murray, S. Rathee, and B.G. Fallone. (2010). "Lung dosimetry in a linac-MR radiotherapy unit with a longitudinal magnetic field." *Med. Phys.* 37: 4722–32.
- Kirkby, C., T. Stanescu, S. Rathee, M. Carlone, B. Murray, and B.G. Fallone. (2008). "Patient dosimetry for hybrid MRI-radiotherapy systems." *Med. Phys.* 35:1019–27.)
- Legendijk, J.J.W., B.W. Raaymakers, A.J.E. Raaijmakers, J. Overweg, K.J. Brown, E.M. Kerkhof, R.W. van der Put, B. Hardemark, M. van Vulpen, and U.A. van der Heide. (2008). "MRI/linac integration." *Radiother. Oncol.* 86: 25–29.
- Lamey, M., B. Burke, E. Blosser, S. Rathee, N. De Zanche, and B.G. Fallone. (2010). "Radio frequency shielding for a linac-MR system." *Phys. Med. Biol.* 55:995–1006.
- Litzenberg, D.W., B.A. Fraass, D.L. McShan, T.W.O. O'Donnell, D.A. Roberts, F.D. Becchetti, A.F. Bielajew, and J.M. Moran. (2001). "An apparatus for applying strong longitudinal magnetic fields to clinical photon and electron beams." *Phys. Med. Biol.* 46:N105–15.
- Low, D.A., W.B. Harms, M. Mutic, and J.A. Purdy. (1998). "A technique for the quantitative evaluation of dose distributions." *Med. Phys.* 25:656–61.
- Meijsing, I., B.W. Raaymakers, A.J.E. Raaijmakers, J.G.M. Kok, L. Hogeweg, B. Liu, and J.J.W. Legendijk. (2009). "Dosimetry for the MRI accelerator: the impact of a magnetic field on the response of a Farmer NE2571 ionization chamber." *Phys. Med. Biol.* 54:2993–3002.
- Meyer, R.A., F.L. Bouquet, and R.S. Alger. (1956). "Radiation induced conductivity in polyethylene and Teflon." *J. Appl. Phys.* 27:1012–18.
- Nioutsikou, E., Y. Seppenwoolde, J.R.N. Symonds-Taylor, B. Heijmen, P. Evans, and S. Webb. (2008). "Dosimetric investigation of lung tumor motion compensation with a robotic respiratory tracking system: an experimental study." *Med. Phys.* 35:1232–40.
- Oborn, B.M., P.E. Metcalfe, M.J. Butson, and A.B. Rosenfeld. (2009). "High resolution entry and exit Monte Carlo dose calculations from a linear accelerator 6 MV beam under the influence of transverse magnetic fields." *Med. Phys.* 36:3549–59.
- Oborn, B.M., P.E. Metcalfe, M.J. Butson, and A.B. Rosenfeld. (2010). "Monte Carlo characterization of skin doses in 6 MV transverse field MRI-linac systems: effect of field size, surface orientation, magnetic field strength, and exit bolus." *Med. Phys.* 37:5208–16.
- Raaijmakers, A.J.E., B.W. Raaymakers, S. van der Meer, and J.J.W. Legendijk. (2007). "Integrating a MRI scanner with a 6 MV radiotherapy accelerator: impact of the surface orientation on the entrance and exit dose due to the transverse magnetic fields." *Phys. Med. Biol.* 52:929–39.
- Raaijmakers, A.J., B.W. Raaymakers, and J.J. Legendijk. (2005). "Integrating a MRI scanner with a 6MVradiotherapy accelerator: dose increase at tissue-air interfaces in a lateral magnetic field due to returning electrons." *Phys. Med. Biol.* 50:1363–76.
- Raaijmakers, A.J., B.W. Raaymakers, and J.J. Legendijk. (2008). "Magnetic-field induced dose effects in MR-guided radiotherapy systems: dependence on the magnetic field strength." *Phys. Med. Biol.* 53:909–23.

- Reynolds, M., B. Fallone, and S. Rathee. (2013). "Dose response of selected ion chambers in applied homogeneous transverse and longitudinal magnetic fields." *Med. Phys.* 40:042102.
- Reynolds, M., B.G. Fallone, and S. Rathee. (2014). "Dose response of selected solid state detectors in applied homogeneous transverse and longitudinal magnetic fields." *Med. Phys.* 41:092103.
- Reynolds, M., B.G. Fallone, and S. Rathee. (2015). "Technical note: response measurement for select radiation detectors in magnetic fields." *Med. Phys.* 42:2837–40.
- Rogers, D.W.O., B.A. Faddegon, G.X. Ding, C.M. Ma, J. We, and R. Mackie. (1995). "BEAM – A Monte Carlo code to simulate radiotherapy treatment units." *Med. Phys.* 22:503–24.
- Roy, R., and O. Shanker. (1993). "Calculation of intercavity coupling coefficient for side coupled standing-wave linear accelerator." *IEEE Trans. Microwave Theory Tech.* 41:1233–35.
- Santos, D.M., J. St. Aubin, B.G. Fallone, and S. Steciw. (2012). "Magnetic shielding investigation for a 6 MV in-line linac within the parallel configuration of a linac-MR system." *Med. Phys.* 39:788–97.
- Sheikh-Bagheri, D., W.O. Rogers. (2002). "Sensitivity of megavoltage photon beam Monte Carlo simulations to electron beam and other parameters." *Med. Phys.* 29:379–90.
- Sinha, R., N. Pervez, R. Rivest, A. Heikal, K. Wachowicz, B.G. Fallone, and B. Abdulkarim. (2005). "Multimodality biological imaging alters target definition compared to conventional target definition in glioblastoma multiforme." *Radiother. Oncol.* 78:209.
- Smit, K., B. Asselen, J.G.M. Kok, J.J.W. Lagendijk, and B. Raaymakers. (2012). "TH-E-BRB-09: reference dosimetry for an MRI-linac: the magnetic field correction factor." *Med. Phys.* 39:4010–11.
- St. Aubin, J., A. Keyvanloo, and B.G. Fallone. (2016). "Discontinuous finite element space-angle treatment of the first order linear Boltzmann transport equation with magnetic fields: Application to MRI-guided radiotherapy." *Med. Phys.* 43:195–204.
- St. Aubin, J., A. Keyvanloo, O. Vassiliev, and B.G. Fallone. (2015). "A deterministic solution of the first order linear Boltzmann transport equation in the presence of external magnetic fields." *Med. Phys.* 42:780–93.
- St. Aubin, J., S. Steciw, and B.G. Fallone. (2010a). "The design of a simulated in-line side-coupled 6 MV linear accelerator waveguide." *Med. Phys.* 37:466–76.
- St. Aubin, J., S. Steciw, and B.G. Fallone. (2010b). "Effect of longitudinal magnetic fields on a simulated 6 MV linac." *Med. Phys.* 37:4916–23.
- St. Aubin, J., S. Steciw, and B.G. Fallone. (2010c). "Effect of transverse magnetic fields on a simulated in-line 6 MV linac." *Phys. Med. Biol.* 55:4861–69.
- St. Aubin, J., S. Steciw, and B.G. Fallone. (2010d). "An integrated 6 MV linear accelerator model from electron gun to dose in a water tank." *Med. Phys.* 37:2279–88.
- St. Aubin, J., S. Steciw, and B.G. Fallone. (2010e). "Magnetic decoupling of the linac in a low field biplanar linac-MR system." *Med. Phys.* 37:4755–61.
- St. Aubin, J., S. Steciw, D-M Santos, and B.G. Fallone. (2010). "Effect of longitudinal magnetic fields on a simulated 6 MV linac." *Med. Phys.* 37:4916–23.
- Steciw, S., T. Stanescu, M. Carlone, and B.G. Fallone. (2007). "TH-C-M100J-01: magnetic shielding of a coupled MRI-linac system." *Med. Phys.* 34:2623.
- Tanabe, E. (1983). "Voltage breakdown in s-band linear accelerator cavities." *IEEE Trans. Nucl. Sci.* 30:3551–53.
- Vedam, S.S., V.R. Kini, P.J. Keall, V. Ramakrishnan, H. Mostafavi, and R. Mohan. (2003). "Quantifying the predictability of diaphragm motion during respiration with a noninvasive external marker." *Med. Phys.* 30: 505–13.
- Wachowicz, K., T. Stanescu, S.D. Thomas, and B.G. Fallone. (2010). "Implications of tissue magnetic susceptibility-related distortion on the rotating magnet in an MR-linac design." *Med. Phys.* 37:1714–21.
- Wachowicz, K., T. Tadic, and B.G. Fallone. (2012). "Geometric distortion and shimming considerations in a rotating MR-linac design due to the influence of low-level external magnetic fields." *Med. Phys.* 39:2659–68.
- Wang, D., W. Strugnell, G. Cowin, D.M. Doddrell, and R. Slaughter. (2004). "Geometric distortion in clinical MRI systems Part I: evaluation using a 3D phantom." *Magn. Reson. Imaging* 22:1211–21.
- Yun, J., E. Yip, Z. Gabos, K. Wachowicz, S. Rathee, and B.G. Fallone. (2015). "Neural-network based autocontouring algorithm for intrafractional lung-tumor tracking using linac-MR." *Med. Phys.* 42:2296.
- Yun, J., J. St. Aubin, S. Rathee, and B.G. Fallone. (2010). "Brushed permanent magnet DC MLC motor operation in an external magnetic field." *Med. Phys.* 37:2131–34.
- Yun, J., K. Wachowicz, M. Mackenzie, S. Rathee, D. Robinson, and B.G. Fallone. (2013). "First demonstration of intrafractional tumor-tracked irradiation using 2D phantom MR images on a prototype linac-MR." *Med. Phys.* 40:051718.
- Yun, J., M. Mackenzie, S. Rathee, D. Robinson, and B.G. Fallone. (2012). "An artificial neural network (ANN)-based lung-tumor motion predictor for intrafractional MR tumor tracking." *Med. Phys.* 39:4423–33.